Where Water is Oxidized to Dioxygen:

Structure of the Photosynthetic Mn$_4$Ca Cluster from X-ray Spectroscopy

Junko Yano* and Vittal K. Yachandra*

Physical Biosciences Division, Lawrence Berkeley National Laboratory,

Berkeley, CA 94720, USA

*To whom correspondence should be addressed: Tel: 510 486 4366, JYano@LBL.GOV; Tel: 510 486 4963, VKYachandra@LBL.GOV; http://www.lbl.gov/~vkyachan/index.html

Abstract

Light-driven oxidation of water to dioxygen in plants, algae and cyanobacteria is catalyzed within photosystem II (PS II) by a Mn_4Ca cluster. Although the cluster has been studied by many different methods, the structure and the mechanism have remained elusive. X-ray absorption and emission spectroscopy and EXAFS studies have been particularly useful in probing the electronic and geometric structure, and the mechanism of the water oxidation reaction. Recent progress, reviewed here, includes polarized X-ray absorption spectroscopy measurements of PS II single crystals. Analysis of those results has constrained the Mn_4Ca cluster geometry to a set of three similar high-resolution structures. The structure of the cluster from the present study is unlike either the 3.0 or 3.5 Å-resolution X-ray structures or other previously proposed models. The differences between the models derived from X-ray spectroscopy and crystallography are predominantly because of damage to the Mn_4Ca cluster by X-rays under the conditions used for structure determination by X-ray crystallography. X-ray spectroscopy studies are also used for studying the changes in the structure of the Mn_4Ca catalytic center as it cycles through the five intermediate states known as the S_i-states (i=0-4). The electronic structure of the Mn_4Ca cluster has been studied more recently using resonant inelastic X-ray scattering spectroscopy (RIXS), in addition to the earlier X-ray absorption and emission spectroscopy methods. These studies are revealing that the assignment of formal oxidation states is overly simplistic. A more accurate description should consider the charge density on the Mn atoms that includes the covalency of the bonds and delocalization of the charge over the cluster. The geometric and electronic structure of the Mn_4Ca cluster in the S-states derived from X-ray spectroscopy are leading to a detailed understanding of the mechanism of the O-O bond formation during the photosynthetic water splitting process.

I. Introduction

Photosynthetic water oxidation is a fundamental chemical reaction that sustains the biosphere. It takes place at a catalytic Mn_4Ca site within the oxygen-evolving complex (OEC) of photosystem II (PS II), which is embedded in the thylakoid membranes of green plants, cyanobacteria and algae.[1] Life-supporting oxygen, currently present at 20% in Earth's atmosphere, is a consequence of this process by oxygenic photosynthetic organisms that are able to use sunlight as the energy source and water as the primary reductant for the fixation of carbon. Only because of the constant regeneration of oxygen through the photosynthetic water oxidation reaction is it abundant in the atmosphere. Although three billion years of evolution have created many differences between oxygenic photosynthetic organisms, remarkably the OEC has remained, to our current knowledge, practically unchanged.

The heart of the OEC is a cluster of four Mn and one Ca ions (Mn_4Ca) that have been shown by X-ray absorption spectroscopy to be linked by mono- and di-μ-oxo or hydroxo bridges.[2-4] The specific protein environment and probably one chloride are also essential for optimal water splitting activity, which is driven by light-induced charge separation at the P_{680} chlorophyll pigments of the PS II reaction center. During water oxidation the OEC cycles through five different oxidation states (Fig. 1), which are known as S_i-states (i = 0 to 4), coupling the one-electron photochemistry of the reaction center with the four-electron chemistry of water oxidation.[5] The OEC in the cluster undergoes oxidation in response to electron transfers driven by photon absorption by the reaction center pigments. The intermediate oxidized species are sufficiently stable to accumulate the oxidizing equivalents needed for the 4-electron transfer of the final step. Thus, nature avoids releasing harmful chemical intermediates such as superoxide or peroxide during the water oxidation. Once four oxidizing equivalents are accumulated in the

OEC (S_4-state), a spontaneous reaction occurs that results in the release of O_2 and the formation of the S_0-state.

The structure of the catalytic Mn_4Ca complex has been the subject of intense study ever since Mn was identified as an essential element for oxygenic photosynthesis.[1,2,6-9] The critical questions related to this process concern the structural and electronic state and the changes in the Mn_4Ca complex as the OEC proceeds through the S-state cycle. The urgent need to develop renewable energy resources that are essentially carbon neutral has highlighted the importance of learning how water is oxidized to oxygen during photosynthesis.[10] The focus of this review is on recent results from our laboratory that address these questions, using polarized EXAFS of single crystals of PS II,[11] range-extended EXAFS,[12,13] and resonant inelastic X-ray spectroscopy (RIXS).[14,15]

II. Structure of the Mn_4Ca Cluster in Photosynthesis

A. Single Crystal X-ray Spectroscopy

A key to understanding the mechanism of water oxidation by the OEC in PS II is the determination of the structure of the Mn_4Ca cluster, which has eluded both Mn X-ray absorption fine structure (EXAFS)[3,4,16,17] and X-ray diffraction (XRD) studies[18-22] until now. XRD studies have provided critical information about its structure; however, even the XRD data of the highest resolution presently available at 3.0 Å are insufficient to accurately determine the positions of Mn, Ca and the bridging and terminal ligands. This is reflected by the differences in the placement of the metal ions and putative ligands in the 3.0[22] and 3.5 Å[21] structures. Moreover, there is a serious concern of X-ray induced damage to the Mn_4Ca cluster; hence, it is important to review the issue of the X-ray dose used in X-ray crystallography and spectroscopy studies.

Therefore, before addressing the issue of Mn_4Ca models derived from single-crystal X-ray spectroscopy,[11] we present a brief review of the Mn XANES and EXAFS data that are directly relevant to the problem of X-ray damage to the Mn_4Ca cluster.[23] It is a case study for other redox-active metallo-proteins.

Damage by X-rays: A Case Study for Metallo-Protein Crystallography. At present there are discrepancies among the models of the structure of the Mn_4Ca complex in the published X-ray crystallography studies, and inconsistencies with X-ray,[24-26] EPR[27-29] and FTIR[30-32] spectroscopy data (Fig. 2). This disagreement is predominantly a function of X-ray-induced damage to the catalytic metal site.

It is therefore imperative to monitor the X-ray-induced effects on the electronic and geometric structure of the Mn_4Ca complex *in-situ* to monitor the X-ray-induced damage or lack thereof of the Mn_4Ca complex to validate the structures based on X-ray crystallography.

In order to determine a safe level of X-ray dose for our single-crystal X-ray spectroscopy studies, we conducted a comprehensive survey of the effects of radiation dose, energy of the X-rays, and temperature of irradiation on the structure of the Mn_4Ca cluster in single-crystals and solutions of PS II.[23] These studies have revealed that the conditions used for structure determination by X-ray diffraction methods are damaging to the metal-site structure as monitored by XANES and EXAFS spectroscopy, for both cyanobacteria and spinach at room and lower temperatures.[23,33] With the advent of third-generation synchrotron sources, the intensity of X-rays available for crystallography has increased considerably, and X-ray damage to biomolecules has been a continuing concern. This is a well recognized problem, and various steps have been taken to minimize such damage.[34] In most crystallography studies it is the loss of diffractivity as evidenced by loss of resolution that is used as a measure of X-ray damage.[35]

However, as shown in our study,[23] this method is not sensitive to localized damage as is prevalent in redox-active metal-containing proteins. We used *in situ* XANES and EXAFS to show that for the Mn_4Ca cluster in PS II the damage to the metal site precedes the loss of diffractivity by more than an order of magnitude of X-ray dose. Because structure-function correlations are routinely made using the structures determined by X-ray crystallography, it is important to know that the metal-site structures are indeed intact. This is particularly important for radiation-sensitive metallo-proteins.

The Mn XANES data from PS II single crystals show that, following X-ray doses characteristic of the XRD measurements, Mn is reduced to $Mn(II)$ from $Mn_4(III_2, IV_2)$ present in the S_1-state (Fig. 3). The reduction of Mn is similar in PS II crystals (Fig. 3A) and in solution (Fig. 3B), and the quantity of $Mn(II)$ can be accurately quantitated as shown in the Fig. 3C. Fig. 3D shows typical XANES spectra from Mn complexes in oxidation states II, III and IV. The X-ray dose used for exposure is from $0.14 - 5.0 \times 10^{10}$ photons/μm^2 (light-blue to black lines, Fig. 3A). An average dose of $\sim 3.5 \times 10^{10}$ photons/μm^2 was used for X-ray diffraction studies. The exposure was at 100 K, and all XANES was collected at 10 K at low dose ($1 \times 10^7/\mu m^2$). XANES and difference spectra show that the increase in amplitude at ~ 6552 eV provides definite evidence for the photo-reduction to $Mn(II)$ in PS II crystals by exposure to X-rays. At a dose of 2.3×10^{10} photons/μm^2, equal to 66% of the average dose used for diffraction measurements, 80% of the Mn in PS II is present as $Mn(II)$. The damage results are summarized in Fig. 4. The dose on the abscissa is given in Grays and in photons/unit area, units that are commonly used for crystallography and spectroscopy experiments, respectively.

In addition to Mn reduction, the EXAFS spectrum changes significantly at the dose that was used for X-ray crystallography experiments. The spectrum changes from one that is

characteristic of a multinuclear oxo-bridged Mn_4Ca complex to one that is typical of mononuclear hexa-coordinated Mn(II) in solution (Fig. 5).[23] The three Fourier peaks (Fig. 5, left in red) are characteristic of a bridged Mn_4Ca complex. Peak I derives from bridging Mn-oxo and Mn-terminal ligand atoms, peak II is from Mn-Mn distances at 2.7 Å characteristic of di-μ-oxo bridged moieties and peak III is from mono-μ-oxo bridged Mn-Mn distances at 3.3 Å and Mn-Ca distances at 3.4 Å. The dosages corresponding to A, B, C and D are labeled in Fig. 4. The Fourier peaks exhibit drastic changes as the percent of Mn(II) increases. Peak II and peak III (vertical dashed gray lines) that are characteristic of Mn-Mn, distances at 2.7, 3.3 and 3.4 Å decrease and disappear along with peak I that is due to Mn-oxo bridging atoms. At the same time, the appearance of a longer Mn-ligand interaction at 2.2 Å is observed. The EXAFS modulations (Fig. 5 right) from the intact PS II spectrum contain several sinusoidal components, as expected from a bridged multinuclear Mn_4Ca complex. The spectrum of sample D is significantly different in both frequency and phase of the modulations with just one sinusoidal oscillation, as one would expect from a symmetric hexa-coordinated Mn(II) species with one shell of backscattering atoms. The spectra from samples A, B and C are intermediate, with considerable damping in the amplitude and changes in the frequency components to the spectra. The results are similar for PS II solution and crystal samples.

These X-ray spectroscopy results present clear evidence that there are no specific metal-bridging or metal-metal interactions in PS II samples irradiated at the average dose used for X-ray crystallography. This is shown by the disappearance of the Fourier peaks that are characteristic of Mn-bridging oxo, and Mn-Mn/Mn-Ca interactions with di-μ-oxo or mono μ-oxo bridges, and by the appearance of Mn-O distances characteristic of Mn(II)-O ligand bond lengths.

The density seen in the X-ray diffraction results is in all probability from the Mn(II)-hexa coordinated ions that are distributed in the binding pocket, presumably bound to carboxylate ligands and free water. This produces a distribution of metal binding sites and the resultant unresolved electron density.

These studies reveal that the conditions used for structure determination by X-ray crystallography cause serious damage specifically to the metal-site structure, resulting not only in the reduction of Mn (Figs. 3, 4) but in the disruption of the bridged Mn structure (Fig. 5). The results show furthermore that the damage to the active metal site occurs at a much lower X-ray dose than that causing the loss of diffractive power of the crystals as established by X-ray crystallography. The damage is significantly higher at wavelengths used for anomalous diffraction measurements and is much lower at liquid He temperatures (10 K) compared to 100 K, where the crystallography experiments were conducted (Fig. 4). For future X-ray crystallography work on the Mn_4Ca complex it will therefore be imperative to develop protocols that mitigate the X-ray induced damage. More generally, these data show that in redox-active metalloproteins careful evaluations of the structural intactness of the active site(s) is required before structure-function correlations can be made on the basis of high resolution X-ray crystal structures.

Structure of the Mn₄Ca Complex from Polarized EXAFS of PS II Crystals. PS II membranes can be oriented on a substrate such that the membrane planes are roughly parallel to the substrate surface. This imparts a one-dimensional order to these samples; while the *z* axis for each membrane (collinear with the membrane normal) is roughly parallel to the substrate normal, the *x* and *y* axes remain disordered.[36] Exploiting the plane-polarized nature of synchrotron radiation, spectra can be collected at different angles between the substrate normal and the X-ray

e-vector. The dichroism of the absorber-backscatterer pair present in the oriented samples is reflected in, and can be extracted from, the resulting X-ray absorption spectra.[17,24,37-39] This is possible because the EXAFS amplitude is proportional to $\sim\cos^2\theta$, where θ is the angle between the X-ray **e**-vector and the absorber-backscatterer vector. The EXAFS of the oriented PS II samples exhibits distinct dichroism, from which we have deduced the relative orientations of several interatomic vector directions relative to the membrane normal and derived a topological representation of the metal sites in the OEC. However, because the samples are ordered in only one dimension, the dichroism information is available only in the form of an angle with respect to the membrane normal. For EXAFS measurements, this means that the absorber-backscatterer vectors can lie anywhere on a cone defined by the angle the vector forms with the membrane normal.

Further refinement can be performed if samples with three-dimensional order, *i.e.* single crystals, are examined instead of oriented membranes.[40,41] These studies have been able to significantly expand the X-ray absorption spectroscopic information available for these systems over what is gleaned from studies of isotropic samples.

We have developed the methodology for collecting single-crystal XAS data from PS II. XAS spectra were measured at 10 K using a liquid He cryostat or cryostream, and an imaging plate detector placed behind the sample was used for *in situ* collection of diffraction data and determination of the crystal orientation (Fig. 6). EXAFS experiments with PS II require a substantially lower X-ray dose than XRD measurements, and the onset of radiation damage can be precisely determined and controlled by monitoring the Mn K-edge position, thus allowing the collection of data from the intact Mn_4Ca cluster of PSII. In addition, EXAFS provides metal-to-metal and metal-to-ligand distances with high accuracy ($\sim$0.02 Å) and a resolution of $\sim$0.1 Å.

Mn- and Ca-EXAFS studies of frozen solutions of PSII preparations have provided accurate distances and numbers of Mn-Mn, Mn-Ca, and Mn/Ca-ligand vectors in the Mn_4Ca cluster and have led to the development of several possible structural models for the Mn_4Ca cluster

We have reported the polarized EXAFS spectra of oriented PS II single crystals, which result in a set of similar high-resolution structures for the Mn_4Ca cluster (Fig. 7).[11] These were derived from simulations of single-crystal polarized spectra based on the experimentally observed dichroism. These structural models are dependent only on the spectroscopic data and are independent of the electron density from X-ray diffraction studies. In order to discriminate between symmetry-related structural models that are possible because of the presence of a non-crystallographic C_2 axis, the cluster was placed within PS II taking into account the overall shape of the electron density of the metal site and the putative ligand information from X-ray crystallography, including IR and EPR studies. The center of mass of the structural models was translated to the center of electron density attributed to the Mn_4Ca cluster in the 3.0 Å XRD structure.[22] The models were not optimized with respect to the electron density, or rotated with respect to the crystal axes, as that would change the dichroic characteristics. Of the four options shown in Yano et al,[11] it is possible to rule out Model I on the basis of oriented membrane EXAFS data.[13,24] The other three models, II, IIa and III, in the putative ligand environment are shown in Fig. 8A. However, we caution that the ligand positions (Fig. 8B) are tentative, because they are likely to be affected by radiation damage, as are the positions of the metal atoms from XRD.[23,33]

The structure of the Mn_4Ca cluster from the polarized EXAFS study of PS II single crystals is unlike either the 3.0[22] or 3.5 Å[21] resolution X-ray structures and other previously proposed models. The comparison of the experimental data with the polarized EXAFS spectra

calculated for the XRD models at 3.5[21] and 3.0 Å[22] resolution is shown in Fig. 9A. A comparison of Model II from polarized single crystal EXAFS is overlayed from models derived from the X-ray crystal structures at 3.0 and 3.5 Å in Fig. 9B. The disagreement is notable; it is most likely due to the X-ray damage to the Mn_4Ca cluster during XRD measurements.[23] We emphasize that these differences are in the overall structure and orientation of the cluster, and not just in the details of the coordinate positions of the atoms.

The polarized EXAFS study of PS II single crystals demonstrates that the combination of XRD and polarized EXAFS can be used to construct a high-resolution model of the Mn_4Ca cluster, that is not compromised by radiation-induced damage to the cluster.

B. Range-extended X-ray absorption Spectroscopy

EXAFS spectra of metallo-protein samples are normally collected as an excitation spectrum by electronically windowing the Kα emission (2p to 1s) from the metal atom.[42-44] The solid-state detectors used over the past decade have a resolution of 150-200 eV, making it impossible to discriminate the fluorescence of the absorbing atom (Mn in our case for PS II) from that of the following element (Fe in PS II) in the periodic table. Unfortunately, because of the presence of Fe in the PS II samples we have been limited to a k of about 12 Å^{-1}, that places an inherent limit on the resolution of Mn distances to ~0.15 Å, because spatial resolution in EXAFS is inversely related to the spectral range. We have overcome this limitation by using a high resolution crystal monochromator,[45] that has a resolution of 1 eV. Using the crystal monochromator, we were able to collect EXAFS spectra well beyond the Fe K-edge to k=16.5 Å^{-1}, improving the distance resolution to ~0.1 Å (Fig. 10). We have shown the feasibility of the range-extended EXAFS method and collected data without interference from Fe in the sample.[12]

We can now fit two short Mn-Mn distances in the S_1 and S_2 states; while earlier solution EXAFS studies could discern only one distance of ~2.7 Å. We have also collected range-extended polarized EXAFS data using oriented PS II membranes. These studies also show the heterogeneity clearly; the Mn-Mn distance is ~2.7 Å or 2.8 Å depending on the angle the X-ray **e**-vector makes with the membrane normal. Interestingly, for the first time we were able to resolve the FT peak at ~3.3 Å into one Mn-Mn vector at ~3.2 Å and two Mn-Ca vectors at ~3.4 Å that are aligned at different angles to the membrane normal.[13]

In Fig. 11A Fourier transforms (FTs) of the range-extended EXAFS for PS II in isotropic solution and in oriented membranes in S_1 state are compared. Peaks, labeled I, II, III correspond to the shells of backscatterers from the Mn absorber. Peak I contains the Mn-O bridging and terminal interactions, peak II corresponds to the di-μ-oxo-bridged Mn-Mn moieties, and peak III has information about the mono-μ-oxo-bridged Mn-Mn and Mn-Ca interactions. Increased spectral resolution results in the detection of the orientation dependence of peaks II and III.

Figure 11B shows polar plots of the N_{app} plotted (solid circles) with respect to detection angle (θ). By fitting the angle dependence of the amplitude (N_{app}) the number of backscatterers (N_{iso}) and the average orientation <ϕ> for that shell of scatterers can be determined. Analysis of the orientation dependence of the ~2.7 Å Mn-Mn vector results in two Mn-Mn interactions at an average angle of <ϕ> = 61±5°, with respect to the membrane normal. The ~2.8 Å Mn-Mn vector has one Mn-Mn interaction at an angle of <ϕ> = 64±10° with respect to the membrane normal. In this way we independently derived that the three Mn-Mn distances of ~2.7 Å and ~2.8 Å are present in a 2:1 ratio in PS II samples in the S_1 state.

The range-extended EXAFS method allowed us to resolve the complex nature of the Peak III containing at least two peaks, IIIA and IIIB, having different distances of 3.2 Å and 3.4

Å. Previous Ca EXAFS studies of native PS II,[46] Sr EXAFS of Sr-substituted PS II,[47] and Mn EXAFS of Ca-depleted PS II[48,49] have shown the contribution of both Mn-Mn (~3.2 Å) and Mn-Ca (~3.4 Å) vectors to FT peak III. Peak IIIB can be assigned to the Mn-Ca vector and peak IIIA to the Mn-Mn vector; moreover, the dichroic behavior of the peak IIIB is strikingly similar to that reported previously for the Mn-Sr vector.[24] The dichroism of these peaks shows that the Mn-Mn vector at ~3.2 Å is at ~20° to the membrane plane, while the Mn-Ca vector at ~3.4 Å is aligned at ~18° to the membrane normal (Fig. 11C).

We have extended these studies to the S_0 and S_3 intermediate states of the enzymatic cycle, and the preliminary results show that there is a significant change in the structure of the Mn complex in the S_3 state. This result has important implications for choosing between the many mechanisms that have been proposed for the water oxidation reaction. In conjunction with the data from single-crystal XAS studies, these studies promise to reveal the changes that occur in the structure of Mn_4Ca catalyst as it cycles through the S-states and the mechanism of water oxidation.

III. Electronic Structure of the Mn$_4$Ca Cluster

In addition to the geometric structure, a detailed electronic structure of the Mn_4Ca cluster is required before some key questions for understanding the mechanism of photosynthetic water oxidation can be addressed. They are: 1) whether all four oxidizing equivalents necessary to oxidize water to O_2 accumulate on the four Mn ions of the OEC, 2) do ligand-centered oxidations take place before the formation and release of O_2, and 3) what are the oxidation state assignments for the Mn during S-state advancement.[50]

To understand the mechanism of water oxidation in detail, it is crucial to know whether the extracted electrons accompanying each S-state transition are directly derived from bound water, from the Mn atoms, or from any other parts of the OEC.[51] Several spectroscopic methods, such as EPR,[52-58] FTIR,[30-32,59-62] XAS,[2,16,63] and UV spectroscopy,[64] have been used to address the oxidation state of Mn in each S-state (Fig. 1). EPR spectroscopy has shown that the S_0 and S_2 are characterized by spin S=1/2 ground states, exhibiting multiline EPR signals (MLS).[65-69] The S_1 and S_3 are characterized by parallel-polarized EPR signals, indicating integral spin ground states.[70-73]

X-ray absorption near edge structure (XANES) has been used extensively to investigate the oxidation state of Mn during the S-state transition.[74-76] There is a consensus that Mn-centered oxidation occurs during the S_0 to S_1, and S_1 to S_2 transitions. However, there is still controversy concerning the involvement of Mn oxidation in the S_2 to S_3 transition.[50,63,75,76] Within the context of localized oxidation, the formal oxidation state of the native S_1 state has been assigned to $Mn(III_2,IV_2)$ and S_2 to $Mn(III,IV_3)$. Some groups have proposed $Mn(III_3,IV)$ in the S_2 state and therefore $Mn(III_4)$ for the S_1 state,[53,77] although most spectroscopic evidence does not support this assignment.[29,78] Uncertainty remains in the case of the S_0 and S_3 states. In the S_0 state, one of the questions is whether Mn(II) is present, in which case the oxidation states are $Mn (II,III,IV_2)$,[69] or whether the oxidation states are $Mn (III_3,IV)$.[26] In the S_3 state, there is controversy about whether a Mn-centered oxidation occurs,[63,76] or whether a ligand-centered oxidation takes place before O-O bond formation and release of molecular oxygen.[74,75,79,80]

The disagreement concerning the S_2 to S_3 transition has led to two different types of proposed O_2 evolution mechanisms, with one type incorporating the oxidation of ligand or substrate in the S_3 state and the other type invoking Mn oxidation during the S_2 to S_3 transition.[51]

Fundamental differences in the chemistry of O-O bond formation and O_2 evolution exist between these two types of mechanisms.

Mn X-ray absorption K-edge spectroscopy (1s-3d,4p) (XANES) and Kβ X-ray emission spectroscopy (XES) (3p-1s) of Mn, including the newly introduced resonant inelastic X-ray scattering spectroscopy (1s-3d,2p-1s) have been used to address these questions about the oxidation states and the electronic structure of the Mn_4Ca cluster.[50]

A. Mn K-edge absorption and Kβ emission Spectroscopy

The XANES and Kβ XES flash patterns from a comprehensive study[75] are shown in Figure 12 that has led to important conclusions about Mn oxidation states. Both spectroscopies show a clear shift in the spectra between the samples given 0 and 1 flashes. This shift is to higher energy for XANES spectroscopy and lower energy for Kβ XES indicating the presence of Mn oxidation during the S_1 to S_2 transition. The small change between samples given 1 and 2 flashes in both spectroscopies provides strong support for the S_2 to S_3 transition proceeding without a Mn-centered oxidation. On the next transition, $S_3 \rightarrow [S_4] \rightarrow S_0$, O_2 is released, shifting the position of the spectra of samples given 3 flashes to lower energy for XANES spectroscopy and higher energy for Kβ XES. These flash patterns are explained by the proposed oxidation states of the Mn cluster in the S_0, S_1, S_2, and S_3 states, as shown in Fig. 1. These oxidation states are: S_0: $Mn_4(II,III,IV_2)$ or $Mn_4(III_3,IV)$, S_1: $Mn_4(III_2,IV_2)$, S_2: $Mn_4(III,IV_3)$, S_3: $Mn_4(III,IV_3)^\bullet$, where the superscript dot represents an oxidation that is not Mn centered. Recent ^{55}Mn ENDOR studies show that the oxidation states in the S_0 state are $Mn_4(III_3,IV)$.[28,29]

However, one has to be aware that the Mn K-edge position cannot be simply an indicator of the oxidation state. Due to the extent of the metal 4p orbital, this orbital overlaps with p orbitals of the ligands, either through σ- or π-bonding. Consequently, XANES is sensitive not only to the oxidation state but also to the ligand environment of the metal. However, compared to XANES, Kβ XES is primarily dependent on changes in oxidation state rather than differences in the overall ligand environment. This was illustrated by a detailed XANES and XES study of multinuclear Mn complexes prepared in different oxidation states and with different geometric structures.[81,82]

B. X-ray Resonant Raman or Resonant Inelastic X-ray Scattering (RIXS)

The description of the Mn_4Ca cluster in the various S-states in terms of the formal oxidation states is very useful, and Mn K-edge XANES has been the conventional X-ray spectroscopic method for determining the oxidation states. However, it is also important to understand the electronic structure of the Mn cluster in more detail, and we are using the technique of X-ray resonant Raman or X-ray inelastic scattering spectroscopy (RIXS) that has potential for addressing this issue. The RIXS data are collected by scanning the incident energy (1s to 3d/4p absorption (ν) followed by 2p-1s emission (*f*)) to yield two-dimensional plots that can be interpreted along the incident energy axis or the energy transfer axis, which is the difference between the incident and emission energies (Fig. 13).[83] In case of a 3d transition metal ion like Mn, the decay with the highest probability after 1s core hole creation by X-ray absorption is a radiative 2p to 1s transition (therefore, called 1s2p RIXS). This process can be viewed as an inelastic scattering of the incident photon at the Mn atom. The energy difference between the initial state to the intermediate state is equivalent to the K-edge pre-edge transition

(v), and the difference between the initial state and the final state (v-f) is comparable to L-edge spectroscopy. While the K-edge spectrum is a measure of the charge density of the metal, L-edge spectrum has information about the spin state of the metal also, due to the strong (2p, 3d) multiplet interaction. Hence, RIXS is sensitive not only to the metal charge density, but also to the metal spin state. In general, L-edge spectroscopy is difficult for biological samples because of severe radiation damage caused by the higher X-ray absorption at lower energy, and additionally experiments need to be carried out under ultra-high vacuum conditions. In RIXS, L-edge-like spectra are obtained, but the excitation energy is the same as for K-edge spectroscopy. It also allows us measurement of spectra at 10 K in the presence of an exchange gas atmosphere. Hence, RIXS spectroscopy can circumvent some difficulties in the K-edge and L-edge spectroscopy, and the method is suitable for biological samples.

We have compared the spectral changes in the RIXS spectra between the Mn_4Ca cluster in the S-states,[14] Mn oxides,[15] and Mn coordination complexes (Fig. 14). The results indicate clear differences in how the protein environment modulates the Mn atoms, leading to stronger covalency (see below) for the electronic configuration in the Mn_4Ca cluster compared to that in the oxides or coordination complexes.

The RIXS two-dimensional data are best shown as contour plots (Fig. 14A,B,C). The comparison of Mn(II), Mn(III), Mn(IV) and PS II in the S_1 and S_2 states shows that both states contain a mixture of oxidation states Mn(III) and Mn(IV). The integrated cross sections along the Raman or energy transfer axis are the L_3-like edge (2p to 3d) (Fig. 14D, left). The integrated cross sections along the incident energy are the Mn K pre-edge (1s to 3d) transition (Fig. 14D, right). It is clear from Fig. 14 that Mn in the S_1 state contains oxidation states III and IV; thus

providing confirmation, in combination with EPR results, for the (III_2, IV_2) assignment for the S_1 state.

The 1st moment of the spectrum integrated along the incident energy axis (see Fig. 14D) was calculated for all the S-states and compared with the 1st moments obtained from Mn oxides and Mn coordination compounds in formal oxidation states of (II), (III) and (IV).

In RIXS, the 1st moments along the incident energy and energy transfer axes define 'the center of gravity' energy. The 1st moments were calculated for each spectrum using the following equation, 1st moment $= \Sigma E_j I_j / \Sigma I_j$, where, E_j and I_j are the energy and fluorescence intensities of the jth data point.

As observed in Mn oxides, the 1st moment along the incident energy (Mn K pre-edge) increases as the Mn oxidation state increases due to the decrease in charge density on the Mn (Fig. 15A). The 1st moment shift for the series of Mn oxides follows the formal oxidation state in a linear manner. This suggests that the charge density or effective number of 3d electrons, n_{3d}^{eff}, is directly connected to the effective number of unpaired 3d electrons (spins) in these compounds. The concept of using the effective number of electrons, n_{3d}^{eff}, localized on a specific atom has been suggested before by numerous authors (reviewed in Glatzel et al.[83]) to explain spectral shapes in core hole spectroscopy (see below), such as 1s2p RIXS spectroscopy at the K pre-edge. Covalency can also be deduced from the RIXS spectra, as it can be included in ligand field multiplet theory that have been used for simulating the spectra. This is done by considering ligand-to-metal charge transfer using configuration interaction, where the Mn K pre-edge configurations can be described by a $c_1 |1s3d^5\rangle + c_2 |1s3d^{n+1}\underline{L}\rangle$ excited state configuration mixing ($\underline{L}$ denotes a hole in a ligand orbital) where c_1 and c_2 are coefficients describing the magnitude of admixture of the respective configuration (covalency). The coefficients c_1 and c_2 can be derived

18

in a fit of the experimental spectra.[84-86] It can be more illustrative to describe this using an electron density picture, where it can be expanded in terms of atomic orbitals that can be used to determine the charge (and spin) with fractional orbital population numbers because valence electrons in covalent systems are shared between several atoms. We can thus assign an effective number of electrons to the metal ion 3d shell, n_{3d}^{eff}, in the 1s excited state. A more complete description of this is included in Glatzel et al.[14] and references therein.

The interpretation of the 1st moment shift along the energy transfer direction is more complicated, because it is also affected by the final-state interaction. This arises from the (2p, 3d) electron-electron interaction, which is the exchange energy for electrons with parallel spins (see Glatzel *et al.*, 2004 for details[14]).

For Mn coordination compounds, the 1st moment position along the incident energy axis (Mn pre-edge) shifts more towards lower energy compared to those of the Mn oxides (Fig. 15B), which indicates that Mn coordination compounds have much stronger covalency compared to the Mn oxides. The changes per oxidation state in the 1st moment positions are more pronounced between the Mn oxides than those between the Mn coordination compounds consistent with a stronger covalency in the coordination complexes. It is worth noting that the two Mn(III) complexes do not have similar 1st moment positions. This can be explained by the presence of one counter ion in Mn(III)(Cl-Salp). The [Mn(III)(Cl-Salp)(CH$_3$OH)$_2$] is positively charged. When the complex contains a counter ion, it behaves like a more 'oxidized' form than its formal oxidation state; therefore, the energy difference between the Mn(III)(Cl-Salp) and Mn(IV)(sal)$_2$(bipy) is much smaller. This in fact confirms that the 1st moment analysis reflects the effective number of electrons on Mn.

The 1st moment of the incident energy for PS II is lower than those for the Mn(IV) coordination complex and larger than or similar to those for the Mn(III) coordination complexes (Fig. 15B), which supports the mixed oxidation states of Mn (III) and Mn(IV) in the S$_1$ and S$_2$ states assigned earlier by the EPR and XANES studies. As observed in the PS II S$_1$ and S$_2$ contour plots and line plots (Fig. 14), the spectral changes during the S$_1$ to S$_2$ transition is subtle due to the oxidation state changes of one Mn out of four Mn. The 1st moment shift between S$_1$ and S$_2$ states is a factor of 7-8 smaller than that between Mn(III)(acac)$_3$ and Mn(IV)(Sal)$_2$(bipy). The magnitude of the spectral change "per Mn ion" between Mn(III)(acac)$_3$ and Mn(IV)(Sal)$_2$(bipy) (both are neutral complexes, without any counter-ion) is twice as large as that between the S$_1$ to S$_2$ states, when we consider that there are four Mn present in PS II.

We thus find that the electron that is extracted from the OEC in PS II between S$_1$ and S$_2$ is strongly delocalized, consistent with strong covalency for the electronic configuration in the OEC. The data collection of the S$_0$ and S$_3$ RIXS spectra is currently in progress (unpublished data). The preliminary result indicates that the S$_0$ spectrum has a weaker peak compared to the S$_1$ state, having a more pronounced low energy component. In the S$_2$ to S$_3$ transition, peak intensity becomes stronger and the spectral feature is altered. The orbital population change Δn_{3d}^{eff} per change in oxidation state between the S$_2$ and S$_3$ states is half as much as that between S$_0$ and S$_1$, or S$_1$ and S$_2$ transitions, indicating that the electron is removed from a more covalent form or even more delocalized orbital during this transition.

IV. Mechanism of Photosynthetic Water Oxidation

There are many proposed mechanisms for the photosynthetic water oxidation reaction and the formation of the all important O-O bond.[51,87,88] The two favored mechanisms for water

oxidation by the OEC are: i) nucleophilic attack on a $Mn(V) \equiv O$ or $Mn(IV)=O^{\bullet}$ terminal ligand by Ca bound water or hydroxide;[89] or ii) reaction of a bridging/terminal Mn-oxo unit with predominant radical character with an oxo/hydroxo/water ligand of Ca/Mn or an exogenous H_2O.[79]

The RIXS data shows that the trend for the OEC/Mn_4Ca cluster as it is oxidized is towards more delocalization of charge. These data,[50] along with other studies,[75,90-92] run counter to the idea of one highly charged Mn(V) in the cluster as an intermediate involved in water oxidation. Most $Mn(V) \equiv O$ complexes known at present are all low-spin,[93,94] contrary to the Mn cluster in PS II which is high-spin all the way to the S_3 state.[65-70,72,73,95-100] It has also been noted that breaking a $Mn(V) \equiv O$ bond, a prerequisite for the release of dioxygen, would be more difficult from a low spin configuration.

The structural changes observed by EXAFS during the S_2 to S_3 as observed in the Mn-Mn[79] and Mn-Ca(Sr)[101] distances are significant. It is hard to rationalize such structural changes in the Mn-Mn/Ca distances without significant involvement of the bridging O atoms.

We hypothesize that during the S_2 to S_3 transition the oxidation is predominantly from a bridging oxygen ligand triggering the structural changes in the OEC. We think that the observed structural changes in the S_2 to S_3 transition are compatible with primarily a ligand centered oxidation. It is hard to rationalize the changes in the Mn-Mn and Mn-Ca distances during the S state transitions, especially during the S_2 to S_3 transition, without significant involvement of the bridging O atoms. Theoretical analysis of the OEC indicate that the formation of a low-lying ligand oxygen radical precursor state may be required for forming the O-O bond.[102,102,103] To reach this state, a structural rearrangement is needed at the S_2 to S_3 transition and the changes in the Mn-Mn distances require a model that involves a bridging oxygen atom.

Future Studies

As presented in this review, the combination of XRD and polarized EXAFS on single crystals has several advantages for unravelling structures of X-ray damage-prone, redox-active metal sites in proteins. X-ray crystal structures at medium resolution are sufficient to determine the overall shape and placement of the metal site within the ligand sphere, and refinement by means of polarized EXAFS can provide accurate metal-to-metal and metal-to-ligand vectors. In addition, different intermediate states of the active site (including different metal oxidation states), which may be difficult to study with X-ray crystallography at high resolution, can be examined. The role of ligands in determining the structure and activity of the cluster is also a subject for X-ray spectroscopic investigations using site-directed mutants. The structural model from polarized EXAFS from the S_1 state presented here will provide a framework for studying the structure of the higher S-states. The study of the structural and electronic structure changes in the catalytic Mn_4Ca cluster in the higher S-states of solution and crystals by X-ray spectroscopic methods, now underway, promises to provide a reliable foundation for the investigation of the mechanism of the O-O bond formation during photosynthetic water oxidation. Understanding natures design in the structure of the Mn_4Ca cluster and the mechanism of water oxidation will inform in the design of biomimetic catalysts for water splitting.

Acknowledgements

References

1. Wydrzynski, T.; Satoh, S., *Photosystem II: The Light-Driven Water:Plastoquinone Oxidoreductase*. Springer: Dordrecht, 2005.

2. Yachandra, V. K.; Sauer, K.; Klein, M. P., *Chem. Rev.* **1996,** *96*, 2927-2950.

3. Sauer, K.; Yano, J.; Yachandra, V. K., *Coord. Chem. Rev.* **2007**, In Press.

4. Penner-Hahn, J. E., *Struct. Bond.* **1998,** *90*, 1-36.

5. Kok, B.; Forbush, B.; McGloin, M., *Photochem. Photobiol.* **1970,** *11*, 457-476.

6. Sauer, K., *Acc. Chem. Res.* **1980,** *13*, 249-256.

7. Debus, R. J., *Biochim. Biophys. Acta* **1992,** *1102*, 269-352.

8. Rutherford, A. W.; Zimmermann, J.-L.; Boussac, A., Oxygen Evolution. In *The Photosystems: Structure, Function, and Molecular Biology*, Barber, J., Ed. Elsevier: Amsterdam, 1992; pp 179-229.

9. Ort, D. R.; Yocum, C. F., *Oxygenic Photosynthesis: The Light Reactions.* Kluwer Academic Publishers: Dordrecht, 1996.

10. Lewis, N. S.; Nocera, D. G., *Proc. Natl. Acad. Sci. USA.* **2006,** *103*, 15729-15735.

11. Yano, J.; Kern, J.; Sauer, K.; Latimer, M.; Pushkar, Y.; Biesiadka, J.; Loll, B.; Saenger, W.; Messinger, J.; Zouni, A.; Yachandra, V. K., *Science* **2006,** *314*, 821-825.

12. Yano, J.; Pushkar, Y.; Glatzel, P.; Lewis, A.; Sauer, K.; Messinger, J.; Bergmann, U.; Yachandra, V. K., *J. Am. Chem. Soc.* **2005,** *127*, 14974-14975.

13. Pushkar, Y.; Yano, J.; Glatzel, P.; Messinger, J.; Lewis, A.; Sauer, K.; Bergmann, U.; Yachandra, V. K., *J. Biol. Chem.* **2007,** *282*, 7198-7208.

14. Glatzel, P.; Bergmann, U.; Yano, J.; Visser, H.; Robblee, J. H.; Gu, W. W.; de Groot, F. M. F.; Christou, G.; Pecoraro, V. L.; Cramer, S. P.; Yachandra, V. K., *J. Am. Chem. Soc.* **2004,** *126*, 9946-9959.

15. Glatzel, P.; Yano, J.; Bergmann, U.; Visser, H.; Robblee, J. H.; Gu, W.; de Groot, F. M. F.; Cramer, S. P.; Yachandra, V. K., *J. Phys. Chem. Solid.* **2005,** *66*, 2163-2167.

16. Yachandra, V. K., The Catalytic Manganese-Cluster: Organization of the Metal Ions. In *Photosystem II: The Light-Driven Water:Plastoquinone Oxidoreductase*, Wydrzynski, T.; Satoh, S., Eds. Springer: Dordrecht, 2005; Vol. 22, pp 235-260.

17. Dau, H.; Iuzzolino, L.; Dittmer, J., *Biochim. Biophys. Acta* **2001,** *1503*, 24-39.

18. Zouni, A.; Witt, H.-T.; Kern, J.; Fromme, P.; Krauß, N.; Saenger, W.; Orth, P., *Nature* **2001,** *409*, 739-743.

19. Kamiya, N.; Shen, J. R., *Proc. Natl. Acad. Sci. USA.* **2003,** *100*, 98-103.

20. Biesiadka, J.; Loll, B.; Kern, J.; Irrgang, K. D.; Zouni, A., *Phys. Chem. Chem. Phys.* **2004,** *6*, 4733-4736.

21. Ferreira, K. N.; Iverson, T. M.; Maghlaoui, K.; Barber, J.; Iwata, S., *Science* **2004,** *303*, 1831-1838.

22. Loll, B.; Kern, J.; Saenger, W.; Zouni, A.; Biesiadka, J., *Nature* **2005,** *438*, 1040-1044.

23. Yano, J.; Kern, J.; Irrgang, K.-D.; Latimer, M. J.; Bergmann, U.; Glatzel, P.; Pushkar, Y.; Biesiadka, J.; Loll, B.; Sauer, K.; Messinger, J.; Zouni, A.; Yachandra, V. K., *Proc. Natl. Acad. Sci. USA* **2005,** *102*, 12047-12052.

24. Cinco, R. M.; Robblee, J. H.; Messinger, J.; Fernandez, C.; Holman, K. L. M.; Sauer, K.; Yachandra, V. K., *Biochemistry* **2004,** *43*, 13271-13282.

25. Dau, H.; Liebisch, P.; Haumann, M., *Phys. Chem. Chem. Phys.* **2004,** *6*, 4781-4792.

26. Robblee, J. H.; Messinger, J.; Cinco, R. M.; McFarlane, K. L.; Fernandez, C.; Pizarro, S. A.; Sauer, K.; Yachandra, V. K., *J. Am. Chem. Soc.* **2002,** *124*, 7459-7471.

27. Peloquin, J. M.; Campbell, K. A.; Randall, D. W.; Evanchik, M. A.; Pecoraro, V. L.; Armstrong, W. H.; Britt, R. D., *J. Am. Chem. Soc.* **2000,** *122*, 10926-10942.

28. Kulik, L. V.; Epel, B.; Lubitz, W.; Messinger, J., *J. Am. Chem. Soc.* **2005,** *127*, 2392-2393.

29. Kulik, L. V.; Epel, B.; Lubitz, W.; Messinger, J., *J. Am. Chem. Soc.* **2007**, In press.

30. Debus, R. J.; Strickler, M. A.; Walker, L. M.; Hillier, W., *Biochemistry* **2005,** *44*, 1367-1374.

31. Kimura, Y.; Mizusawa, N.; Ishii, A.; Nakazawa, S.; Ono, T., *J. Biol. Chem.* **2005,** *280*, 37895-37900.

32. Chu, H. A.; Hillier, W.; Debus, R. J., *Biochemistry* **2004,** *43*, 3152-3166.

33. Grabolle, M.; Haumann, M.; Muller, C.; Liebisch, P.; Dau, H., *J. Biol. Chem.* **2006,** *281*, 4580-4588.

34. Garman, E., *Curr. Opin. Struct. Biol.* **2003,** *13*, 545-551.

35. Henderson, R., *Philos. Trans. R. Soc. Lond. Ser. B-Biol. Sci.* **1990,** *241*, 6-8.

36. Rutherford, A. W., *Biochim. Biophys. Acta* **1985,** *807*, 189-201.

37. Mukerji, I.; Andrews, J. C.; DeRose, V. J.; Latimer, M. J.; Yachandra, V. K.; Sauer, K.; Klein, M. P., *Biochemistry* **1994,** *33*, 9712-9721.

38. Dau, H.; Andrews, J. C.; Roelofs, T. A.; Latimer, M. J.; Liang, W.; Yachandra, V. K.; Sauer, K.; Klein, M. P., *Biochemistry* **1995,** *34*, 5274-5287.

39. George, G. N.; Prince, R. C.; Cramer, S. P., *Science* **1989,** *243*, 789-791.

40. Flank, A. M.; Weininger, M.; Mortenson, L. E.; Cramer, S. P., *J. Am. Chem. Soc.* **1986,** *108*, 1049.

41. Scott, R. A.; Hahn, J. E.; Doniach, S.; Freeman, H. C.; Hodgson, K. O., *J. Am. Chem. Soc.* **1982,** *104*, 5364-5369.

42. Scott, R. A., X-ray absorption spectroscopy. In *Structural and Resonance Techniques in Biological Research*, Rousseau, D. L., Ed. Academic Press: Orlando, 1984; pp 295-362.

43. Cramer, S. P., Biochemical Applications of X-ray Absorption Spectroscopy. In *X-ray Absorption: Principles, Applications and Techniques of EXAFS, SEXAFS, and XANES*, Koningsberger, D. C.; Prins, R., Eds. Wiley-Interscience: New York, 1988; pp 257-326.

44. Yachandra, V. K., *Methods Enzymol.* **1995,** *246*, 638-675.

45. Bergmann, U.; Cramer, S. P., A high-resolution large-acceptance analyzer for x-ray fluorescence and Raman spectroscopy. In *SPIE Conference on Crystal and Multilayer Optics*, SPIE: San Diego, CA, 1998; Vol. 3448, pp 198-209.

46. Cinco, R. M.; Holman, K. L. M.; Robblee, J. H.; Yano, J.; Pizarro, S. A.; Bellacchio, E.; Sauer, K.; Yachandra, V. K., *Biochemistry* **2002,** *41*, 12928-12933.

47. Cinco, R. M.; Robblee, J. H.; Rompel, A.; Fernandez, C.; Yachandra, V. K.; Sauer, K.; Klein, M. P., *J. Phys. Chem. B* **1998,** *102*, 8248-8256.

48. Latimer, M. J.; DeRose, V. J.; Mukerji, I.; Yachandra, V. K.; Sauer, K.; Klein, M. P., *Biochemistry* **1995,** *34*, 10898-10909.

49. Latimer, M. J.; DeRose, V. J.; Yachandra, V. K.; Sauer, K.; Klein, M. P., *J. Phys. Chem. B* **1998,** *102*, 8257-8265.

50. Yano, J.; Yachandra, V. K., *Photosynth. Res.* **2007,** *92*, 289-303.

51. Messinger, J., *Phys. Chem. Chem. Phys.* **2004,** *6*, 4764-4771.

52. Peloquin, J. M.; Britt, R. D., *Biochim. Biophys. Acta* **2001,** *1503*, 96-111.

53. Carrell, T. G.; Tyryshkin, A. M.; Dismukes, G. C., *J. Biol. Inorg. Chem.* **2002,** *7*, 2-22.

54. Brudvig, G. W., *Adv. Chem. Ser.* **1995,** *246*, 249-263.

55. Styring, S. A.; Rutherford, A. W., *Biochemistry* **1988,** *27*, 4915-4923.

56. Ioannidis, N.; Sarrou, J.; Schansker, G.; Petrouleas, V., *Biochemistry* **1998,** *37*, 16445-16451.

57. Ioannidis, N.; Schansker, G.; Barynin, V. V.; Petrouleas, V., *J. Biol. Inorg. Chem.* **2000,** *5*, 354-363.

58. Ioannidis, N.; Nugent, J. H. A.; Petrouleas, V., *Biochemistry* **2002,** *41*, 9589-9600.

59. Chu, H.-A.; Hillier, W.; Law, N. A.; Babcock, G. T., *Biochim. Biophys. Acta* **2001,** *1503*, 69-82.

60. Kimura, Y.; Mizusawa, N.; Ishii, A.; Ono, T., *Biochemistry* **2005,** *44*, 16072-16078.

61. Kimura, Y.; Mizusawa, N.; Yamanari, T.; Ishii, A.; Ono, T., *J. Biol. Chem.* **2005,** *280*, 2078-2083.

62. Strickler, M. A.; Hillier, W.; Debus, R. J., *Biochemistry* **2006,** *45*, 8801-8811.

63. Iuzzolino, L.; Dittmer, J.; Dörner, W.; Meyer-Klaucke, W.; Dau, H., *Biochemistry* **1998,** *37*, 17112-17119.

64. Dekker, J. P., Optical studies on the oxygen-evolving complex of photosystem II. In *Manganese Redox Enzymes*, Pecoraro, V. L., Ed. VCH Publishers: New York, 1992; pp 85-103.

65. Dismukes, G. C.; Siderer, Y., *FEBS Lett.* **1980,** *121*, 78-80.

66. Hansson, Ö.; Andréasson, L. E., *Biochim. Biophys. Acta* **1982,** *679*, 261-268.

67. Messinger, J.; Nugent, J. H. A.; Evans, M. C. W., *Biochemistry* **1997,** *36*, 11055-11060.

68. Åhrling, K. A.; Peterson, S.; Styring, S., *Biochemistry* **1998,** *37*, 8115-8120.

69. Messinger, J.; Robblee, J. H.; Yu, W. O.; Sauer, K.; Yachandra, V. K.; Klein, M. P., *J. Am. Chem. Soc.* **1997**, *119*, 11349-11350.

70. Dexheimer, S. L.; Klein, M. P., *J. Am. Chem. Soc.* **1992,** *114*, 2821-2826.

71. Yamauchi, T.; Mino, H.; Matsukawa, T.; Kawamori, A.; Ono, T.-A., *Biochemistry* **1997,** *36*, 7520-7526.

72. Campbell, K. A.; Peloquin, J. M.; Pham, D. P.; Debus, R. J.; Britt, R. D., *J. Am. Chem. Soc.* **1998,** *120*, 447-448.

73. Matsukawa, T.; Mino, H.; Yoneda, D.; Kawamori, A., *Biochemistry* **1999,** *38*, 4072-4077.

74. Roelofs, T. A.; Liang, W.; Latimer, M. J.; Cinco, R. M.; Rompel, A.; Andrews, J. C.; Sauer, K.; Yachandra, V. K.; Klein, M., *Proc. Natl. Acad. Sci. U. S. A.* **1996,** *93*, 3335-3340.

75. Messinger, J.; Robblee, J. H.; Bergmann, U.; Fernandez, C.; Glatzel, P.; Visser, H.; Cinco, R. M.; McFarlane, K. L.; Bellacchio, E.; Pizarro, S. A.; Cramer, S. P.; Sauer, K.; Klein, M. P.; Yachandra, V. K., *J. Am. Chem. Soc.* **2001**, *123*, 7804-7820.

76. Haumann, M.; Muller, C.; Liebisch, P.; Iuzzolino, L.; Dittmer, J.; Grabolle, M.; Neisius, T.; Meyer-Klaucke, W.; Dau, H., *Biochemistry* **2005,** *44*, 1894-1908.

77. Kuzek, D.; Pace, R. J., *Biochim. Biophys. Acta* **2001,** *1503*, 123-137.

78. Yachandra, V. K.; DeRose, V. J.; Latimer, M. J.; Mukerji, I.; Sauer, K.; Klein, M. P., *Science* **1993,** *260*, 675-679.

79. Liang, W.; Roelofs, T. A.; Cinco, R. M.; Rompel, A.; Latimer, M. J.; Yu, W. O.; Sauer, K.; Klein, M. P.; Yachandra, V. K., *J. Am. Chem. Soc.* **2000,** *122*, 3399-3412.

80. Siegbahn, P. E. M., *Chem. Eur. J.* **2006,** *12*, 9217-9227.

81. Visser, H.; Anxolabéhère-Mallart, E.; Bergmann, U.; Glatzel, P.; Robblee, J. H.; Cramer, S. P.; Girerd, J. J.; Sauer, K.; Klein, M. P.; Yachandra, V. K., *J. Am. Chem. Soc.* **2001,** *123*, 7031-7039.

82. Pizarro, S. A.; Glatzel, P.; Visser, H.; Robblee, J. H.; Christou, G.; Bergmann, U.; Yachandra, V. K., *Phys. Chem. Chem. Phys.* **2004,** *6*, 4864-4870.

83. Glatzel, P.; Bergmann, U., *Coord. Chem. Rev.* **2005,** *249*, 65-95.

84. de Groot, F. M. F., *J. Electron Spectrosc. Relat. Phenom.* **1994,** *67*, 529-622.

85. de Groot, F., *Chem. Rev.* **2001,** *101*, 1779-1808.

86. de Groot, F. M. F.; Glatzel, P.; Bergmann, U.; van Aken, P. A.; Barrea, R. A.; Klemme, S.; Havecker, M.; Knop-Gericke, A.; Heijboer, W. M.; Weckhuysen, B. M., *J. Phys. Chem. B* **2005,** *109*, 20751-20762.

87. Renger, G., *Biochim. Biophys. Acta* **2001,** *1503*, 210-228.

88. McEvoy, J. P.; Brudvig, G. W., *Chem. Rev.* **2006,** *106*, 4455-4483.

89. Vrettos, J. S.; Limburg, J.; Brudvig, G. W., *Biochim. Biophys. Acta* **2001,** *1503*, 229-245.

90. Weng, T. C.; Hsieh, W. Y.; Uffelman, E. S.; Gordon-Wylie, S. W.; Collins, T. J.; Pecoraro, V. L.; Penner-Hahn, J. E., *J. Am. Chem. Soc.* **2004,** *126*, 8070-8071.

91. Haumann, M.; Liebisch, P.; Muller, C.; Barra, M.; Grabolle, M.; Dau, H., *Science* **2005,** *310*, 1019-1021.

92. Yano, J.; Robblee, J.; Pushkar, Y.; Marcus, M. A. M.; Bendix, J.; Workman, J. M.; Collins, T. J.; Solomon, E. I.; George, S. D.; Yachandra, V. K., *J. Am. Chem. Soc.* **2007**, *129*, 12989-13000.

93. Workman, J. M.; Powell, R. D.; Procyk, A. D.; Collins, T. J.; Bocian, D. F., *Inorg. Chem.* **1992,** *31*, 1548-1550.

94. Bendix, J.; Deeth, R. J.; Weyhermüller, T.; Bill, E.; Wieghardt, K., *Inorg. Chem.* **2000,** *39*, 930-938.

95. Dismukes, G. C.; Siderer, Y., *Proc. Natl. Acad. Sci. USA* **1981,** *78*, 274-278.

96. Casey, J. L.; Sauer, K., *Biochim. Biophys. Acta* **1984,** *767*, 21-28.

97. Zimmermann, J.-L.; Rutherford, A. W., *Biochim. Biophys. Acta* **1984,** *767*, 160-167.

98. Boussac, A.; Un, S.; Horner, O.; Rutherford, A. W., *Biochemistry* **1998,** *37*, 4001-4007.

99. Horner, O.; Rivière, E.; Blondin, G.; Un, S.; Rutherford, A. W.; Girerd, J.-J.; Boussac, A., *J. Am. Chem. Soc.* **1998,** *120*, 7924-7928.

100. Boussac, A.; Sugiura, M.; Inoue, Y.; Rutherford, A. W., *J. Biol. Chem.* **2000,** *39*, 13788-13799.

101. Pushkar, Y.; Yano, J.; Sauer, K.; Boussac, A.; Yachandra, V. K., (unpublished data).

102. Siegbahn, P. E. M.; Crabtree, R. H., *J. Amer. Chem. Soc.* **1999,** *121*, 117-127.

103. Siegbahn, P. E. M., *Inorg. Chem.* **2000,** *39*, 2923-2935.

104. Wemple, M. W.; Adams, D. M.; Folting, K.; Hendrickson, D. N.; Christou, G., *J. Am. Chem. Soc.* **1995,** *117*, 7275-7276.

105. Cinco, R. M.; Rompel, A.; Visser, H.; Aromi, G.; Christou, G.; Sauer, K.; Klein, M. P.; Yachandra, V. K., *Inorg. Chem.* **1999,** *38*, 5988-5998.

106. Chan, M. K.; Armstrong, W. H., *J. Am. Chem. Soc.* **1991,** *113*, 5055-5057.

107. Chan, M. K. Ph.D. Dissertation, University of California, Berkeley, CA, USA, 1986.

Figure Captions

Figure 1

The S-state cycle and the proposed oxidation states of the Mn cluster in the S-states. The multiline EPR signals for the S_0 and S_2 states and the g-values of the EPR signals identified with S_0, S_1, S_2 and S_3 (for spinach) are also shown.

Figure 2

Structural models of the Mn cluster containing short 2.7 to 2.8 Å Mn-Mn distances characterized by di-μ-oxo bridges and 3.3 Å Mn-Mn distances characterized by mono-μ-oxo bridges. The numbers in parentheses denote the number of short (2.7 to 2.8 Å) and long Mn-Mn ($\sim$3.3 Å) distances, respectively. The topologically equivalent motifs to those proposed from X-ray crystallographic analyses at 3.0 and 3.5 Å are (**A**) on top left[22] and (**B**) right[21], respectively. (**C, D**) Three short (2.7 to 2.8 Å) and one long (3.3 Å) Mn-Mn distances (bottom) are required to satisfy the solution[12,13] and single-crystal EXAFS (bottom).[11] Of these motifs only one option on the extreme right (**D**, bottom) has the requisite numbers of short and long Mn-Mn distances with the correct relative orientation to satisfy the dichroism observed in the single-crystal polarized EXAFS spectra.[11]

Figure 3

A) Mn K-edge shift of PS II crystals as a function of X-ray dose at 13.3 keV (0.933 Å) and 100 K (top), and the difference spectra (below). The spectrum at the highest inflection point energy is from an undamaged PS II crystal.

B) A similar trend in the XANES (top) and the difference spectra (below) is seen for PS II

solutions.

C) The changes in the XANES spectra from an intact PS II sample as a function of addition of 10% increments of the XANES spectrum of aqueous Mn(II) (top), and the corresponding difference spectra (below) (light-blue to black lines). The similarity between the difference spectra in A, B, C is striking, showing the photo-reduction of the $Mn(III_2,IV_2)$ in native PS II to Mn(II).

D) A comparison of Mn K-edge spectra from two tetranuclear complexes, $[Mn_4O_3(OAc)_4(dbm)_3]$[104,105] and $[(Mn_2O_2)_2(tphpn)_2](ClO_4)_4$[106,107] in oxidation states $Mn_4(III_3,IV)$ and $Mn_4(III_2,IV_2)$ and Mn(II) in aqueous solution. The K-edge spectra from the complexes in higher oxidation states are similar to that from an intact PS II sample. The figure was adapted from Yano et al.[23]

Figure 4

Increasing Mn(II) content in PS II due to radiation damage. (Solid blue line) Mn(II) content in PS II crystals as a function of X-ray irradiation at 13.3 keV (0.933 Å). The irradiation was carried out at 100 K. The conditions are similar to those during X-ray diffraction data collection. (Dashed blue line) The damage profile for PS II solution samples is very similar to that seen for crystals, although slightly higher for the same dose. EXAFS spectra of samples shown in Fig. 5 are at levels of damage denoted (on the right) by A, B, C and D (0.05, 0.1, 0.3 and 1.4×10^{10} photons/μm^2 at 13.3 keV and 100 K). An average dose of $\sim 3.5 \times 10^{10}$ photons/μm^2 was used for X-ray diffraction studies. (Dashed green line) The generation of Mn(II) is considerably greater when the X-ray irradiation is at 6.6 keV (1.89 Å) which is the energy at which the anomalous diffraction measurements for PS II were conducted. (Solid blue line) The Mn(II) produced by

damage in crystals is considerably decreased when the irradiation is conducted at 10 K. The figure is adapted from Yano et al.[23]

Figure 5

Spectral changes of PS II Mn EXAFS due to radiation damage.

(left) The Fourier transform of the EXAFS spectrum from an intact PS II solution sample is on top (red). The FTs from PS II solution samples exposed to 0.05, 0.1, 0.3 and 1.4×10^{10} photons/μm^2 at 13.3 keV and 100 K, and containing 25 (blue), 35 (dark blue), 45 (green) and 90% (black) photo-reduced Mn(II) are labeled A, B, C and D respectively. An average dose of $\sim 3.5 \times 10^{10}$ photons/μm^2 was used for X-ray diffraction studies.

(right) Corresponding k^3-space EXAFS spectra of PS II samples. The figure is adapted from Yano et al.[23]

Figure 6

The experimental set-up used for single-crystal X-ray absorption experiments. The PS II crystal was placed in a liquid He cryostat at a temperature of 10 K at ambient pressure. The Mn XANES or EXAFS spectrum was measured as a fluorescence excitation spectrum using a 30-element energy-discriminating solid-state Ge detector placed at 90° to the incident beam. Downstream of the X-ray beam and the PS II crystal is the MAR 345 image plate detector that was used for obtaining the diffraction pattern from which the orientation matrix of the PS II crystal was determined by indexing the reflections. The incident X-ray beam is defined by the slits in the left foreground, and the I_0 ion chamber which is behind the slits is used to measure the intensity of

the incident beam. A shutter that protects the sample from damage during spectrometer motion is behind the ion chamber and before the cryostat.

Figure 7

High-resolution structural models for the Mn_4Ca cluster in PS II from polarized EXAFS. The Mn_4Ca models II. IIa and III (from Yano et al.[11] are shown on the right. Each model is compatible with the polarized Mn EXAFS spectra of single crystals of PS II (see Figure 9A, bottom). The Mn_4 motif common to the three structures is shown at upper left. The models are shown in the orientation in which they should be placed in the PS II membrane according to the axis system shown at upper right. The Mn atoms are shown in red. The distance between Mn_C and Mn_D atoms is ~2.8 Å (indicated by blue oxo bonds), and the distance between the Mn_A and Mn_B atoms, as well as the Mn_B and Mn_C atoms, is ~2.7 Å. The distance between Mn_B and Mn_D is ~3.3 Å. The Ca atom (green sphere) is ~3.4 Å from two Mn atoms. The bridging motif to Ca is not well defined by our experiments; therefore, dashed lines connect the Ca atom to the two Mn atoms at ~3.4 Å. In the middle are the FTs from the calculated polarized EXAFS spectra of the three models, and these compare well with the FTs from the experimental polarized EXAFS spectra shown in the bottom of Fig. 9A.

Figure 8

A) The structural models II, IIa and III are placed in the ligand environment from the X-ray diffraction data of Loll et al.[22] at a resolution of 3.0 Å. The center of mass was translated to the center of electron density attributed to the Mn_4Ca cluster in the XRD structure. This was carried out without any rotation of the models.

B) A schematic diagram of model II with the view along the membrane plane, with putative ligands from the electron density. Bonds between Mn and the bridging oxo are shown as solid green lines. Bonds to putative terminal ligand atoms from amino acids and to Ca atoms are shown as dotted lines (black – <3.0 Å, blue – >3.0 Å).

Figure 9

A) Comparison of the experimental Mn EXAFS dichroism from single-crystals of PS II with the polarized spectrum calculated from the proposed structures from XRD studies. There are clear differences between the experimental spectra shown in the bottom panel and those calculated from the XRD coordinates for the Mn_4Ca cluster at 3.5 Å resolution (top panel)[21] and 3.0 Å resolution (middle panel).[22] The intensity and the dichroism pattern of FT peaks I, II and III (3.5 Å structure) and of FT peaks II and III (3.0 Å structure) are significantly different from the experimental data (bottom panel). For the 3.0 Å resolution structure the μ-oxo bridges were not resolved in the electron density. Hence, only FT peaks II and III, with contributions from Mn and/or Ca, are shown.

B) Comparison of Model II for the Mn_4Ca cluster derived from polarized Mn EXAFS with the models derived from the X-ray crystal structures at 3.0 Å[22] and 3.5 Å[21] resolution. The spheres represent Mn (red), Ca (green) and the bridging oxygen ligand atoms (gray) for Model II from polarized EXAFS of single crystals, and Mn (violet), Ca (cyan) and the bridging oxygen ligand atoms (yellow) for the X-ray crystal structures. (**a**, **b**) Comparison of Model II with the 3.0 Å resolution structure for the Mn_4Ca cluster. **a**: The view is along the membrane plane. **b**: The view is onto the membrane plane from the cytoplasmic (stromal) side. (**c**, **d**) Comparison of Model II

with the 3.5 Å resolution X-ray structure for the Mn_4Ca cluster. **c**: The view is along the membrane plane. **d**: The view is onto the membrane plane from the cytoplasmic side

Figure 10

A) The schematic for the crystal monochromator used in a backscattering configuration.

B) Left: X-ray fluorescence of Mn and Fe, Above: Mn $K\alpha_1$ and $K\alpha_2$ fluorescence peaks, with natural linewidth of ~5 eV, split by 11 eV. The multi-crystal monochromator with 1 eV resolution is tuned to the Mn $K\alpha_1$ peak (red spectrum). Below: fluorescence peaks of Mn and Fe as detected using Ge-detector. The fluorescence peaks are convoluted with the electronic window resolution of 150-200 eV of the Ge detector (black and green spectra for Mn and Fe fluorescence). This method of detection cannot resolve Mn $K\alpha_1$ and $K\alpha_2$ fluorescence peaks. Note different energy scales for the schemes shown above and below. Iron is an obligatory element in functional PS II complexes. Right: Comparison of the PS II Mn K-edge EXAFS spectrum from an S_1 state PS II sample obtained with a traditional 30-element energy-discriminating Ge-detector with a spectrum collected using the high-resolution crystal monochromator. Use of the high-resolution detector eliminates the interference of Fe and removes the limit of the energy range for Mn EXAFS data collection.

Figure 11

A) Fourier Transform (FT) of Mn K-edge EXAFS spectra from isotropic solution and oriented PS II membrane samples in the S_1 state obtained with a high-resolution spectrometer (range-extended EXAFS). Angles indicate orientation of the membrane normal with respect to the X-ray **e**-field vector.

B) Polar plot of the X-ray absorption linear dichroism of PS II samples in the S_1 state. The N_{app} values (solid circles) for oriented membranes are plotted at their respective detection angles (θ). The best fits of N_{app} vs. θ are shown for the various Mn-Mn vectors as solid lines.

C) The orientation of the average Mn-Ca (~3.4 Å) and the Mn-Mn (~3.2 Å) vectors relative to the membrane normal. The figure was adapted from Pushkar et al.[13]

Figure 12

Oscillation of XANES inflection point energies (I.P.E.) and that of first moments (E) of the Kβ emission spectra from the 0F to 3F samples of spinach PS II (BBY). The figure was adapted from Messinger et al., 2001.[75]

Figure 13

(Left) The energy level diagram for the RIXS experiment. The excitation is from a 1s to 3d level (ν), and the emission detected is from a 2p to 1s level (*f*). In RIXS, which is two-dimensional spectroscopy, both the excitation energy (ν) is scanned (1s to 3d and 1s to 4p) using the beamline monochromator and the emission energy (*f*) is scanned across the Ka lines (2p to 1s) with a high resolution analyzer. Both monochromator and analyzer have ~1 eV bandwidth. The difference (ν-*f*) between the incident energy (ν) and the emission energy (*f*) gives the L-edge-like spectrum. Thus using K-edge energies one can collect L-edge-like (2p to 3d) spectra.

(Right) A three-dimensional plot showing the resonant inelastic X-ray spectrum. Abscissa is the excitation energy (ν) across the 1s-3d energy range of the spectrum (K pre-edge). The 1s-3d K-edge fluorescence excitation spectrum is plotted in the back of the three dimensional spectrum

for reference. Ordinate is the difference between the excitation (v) and emission energy (f) (L-edge-like).

Figure 14

A) Contour plots of the $1s2p_{3/2}$ RIXS planes for four Mn oxides in oxidation states II, III and IV, and **B**) the four molecular complexes $Mn^{II}(acac)_2(H_2O)_2$, $Mn^{III}(acac)_3$, $[Mn^{III}(5\text{-}Cl\text{-}Salpn)(CH_3OH)_2]^+$ and $Mn^{IV}(sal)_2(bipy)$, and **C**) the S_1 and S_2 states. Abscissa is the excitation energy and ordinate is the energy transfer axis. **D**) On the left are integrations of the 2D plot parallel to the ordinate which yields L-edge like spectra. The intense feature at 640 eV corresponds to transitions to J=3/2 like states (L_3 edges) and the feature at 655 eV corresponds to J=1/2 like states (L_2 edges). On the right are integrations parallel to the energy transfer axis which yield K pre-edge spectra. The figure was adapted from Glatzel et al., 2004.[14]

Figure 15

A) First moment positions in the $1s2p_{3/2}$ RIXS plane for the Mn oxides, and **B**) the coordination complexes and PS II in S_1 and S_2 states. A linear fit for the Mn oxides is shown as a dotted line in (**A**). The same Mn oxide line is also indicated in (**B**) for a comparison to the slope of Mn coordination complexes and PS II data. Along the incident energy axis the plot gives an ordering of the systems in terms of the effective number of 3d electrons. The figure was adapted from Glatzel et al., 2004.[14]

Figure 1

A

(2, 2)

B

(3, 2)

Mn

O

C

(3, 1)   (3, 1)

D

(3, 1)

Figure 2

Figure 3

Mn(II) Content (%)

100

80

Solution
100K, 6.6keV

Solution
100K, 13.3keV

Crystal
100K, 13.3keV

60

40

Crystal
10K, 13.3keV

20

0

D

C
B
A

0   1.0   2.0   3.0   5.0

Photons (*10^10/μm^2)

(6.6 keV)

0   1.9   3.8   5.7   9.6

0   0.45   0.90   1.35   3.0

(13.3 keV)

Dose (*10^7 Grays)
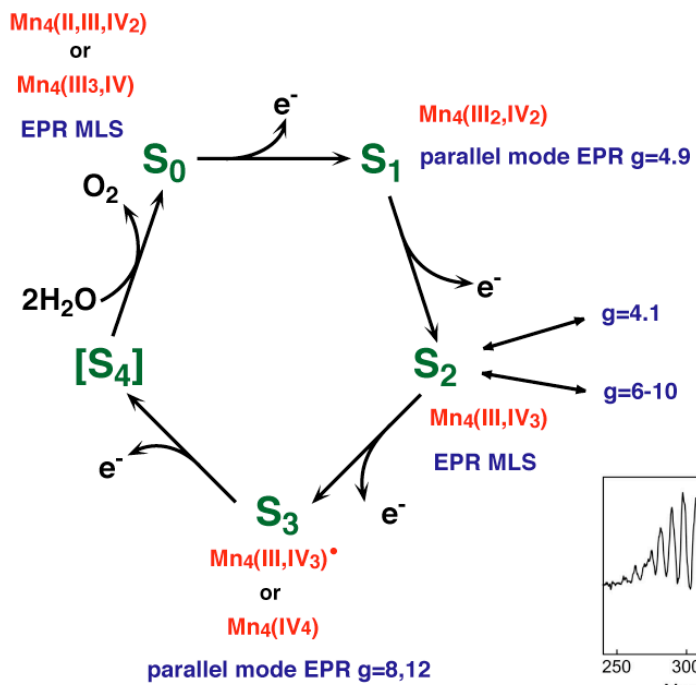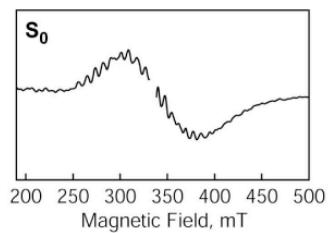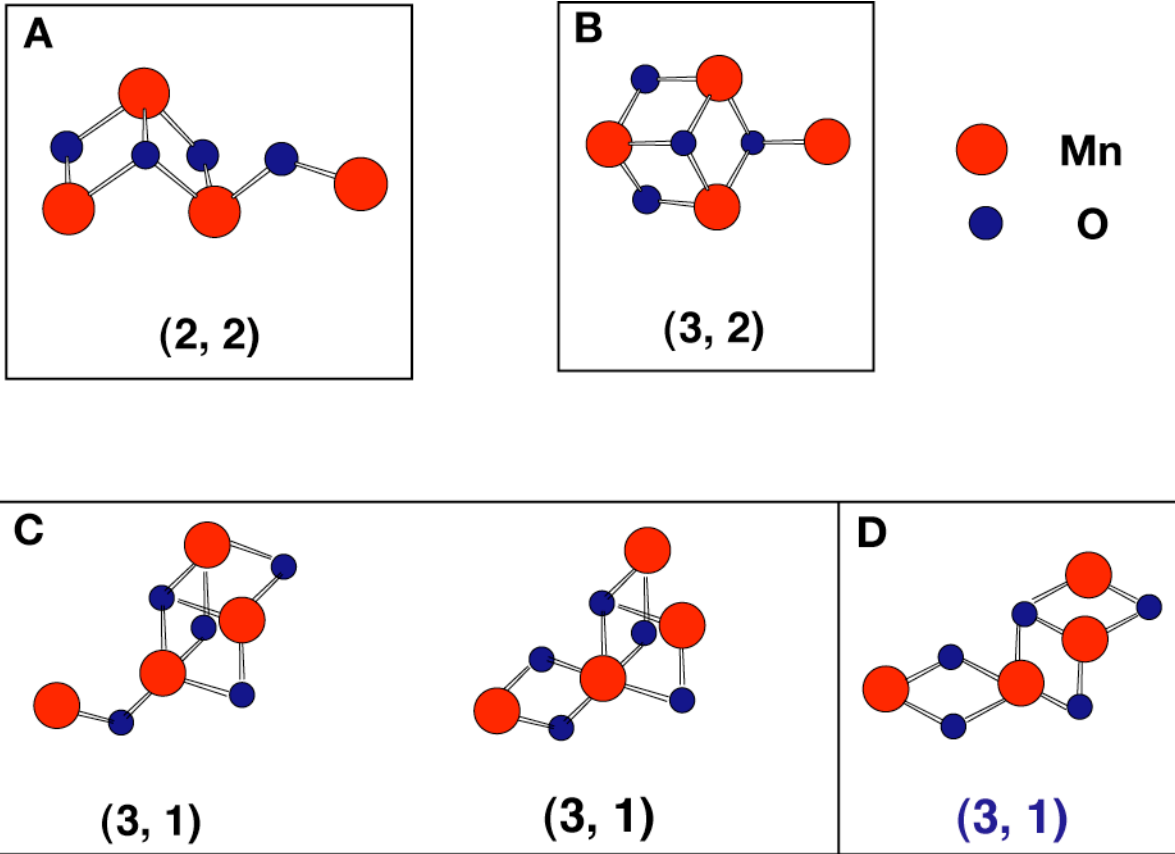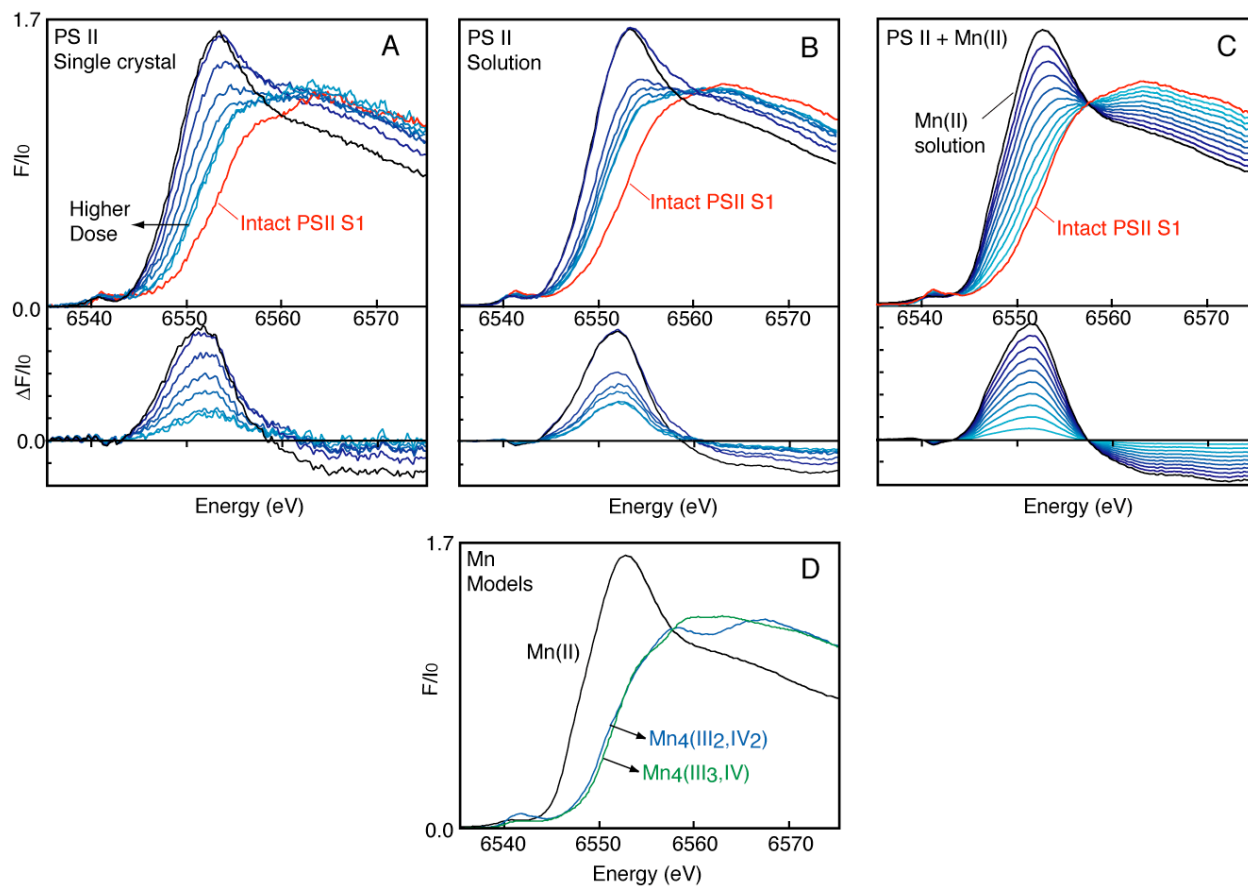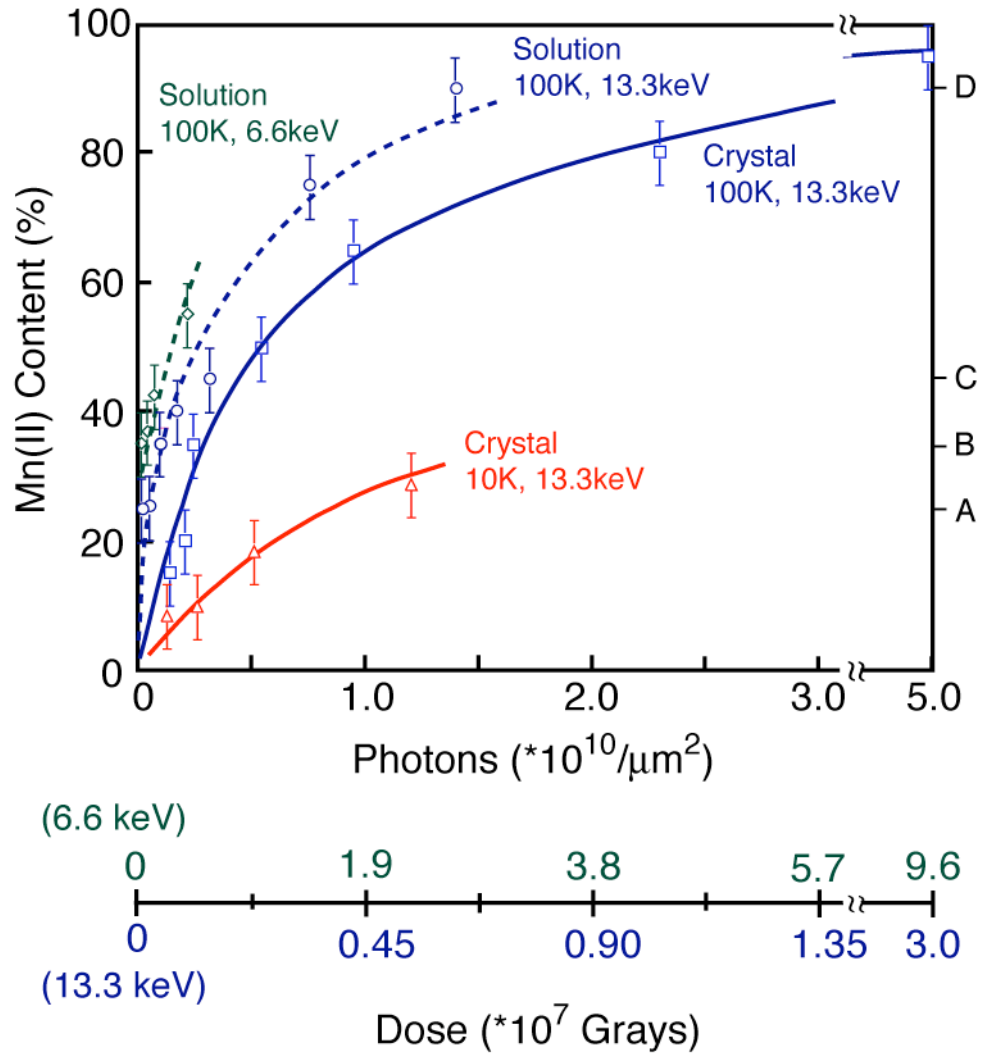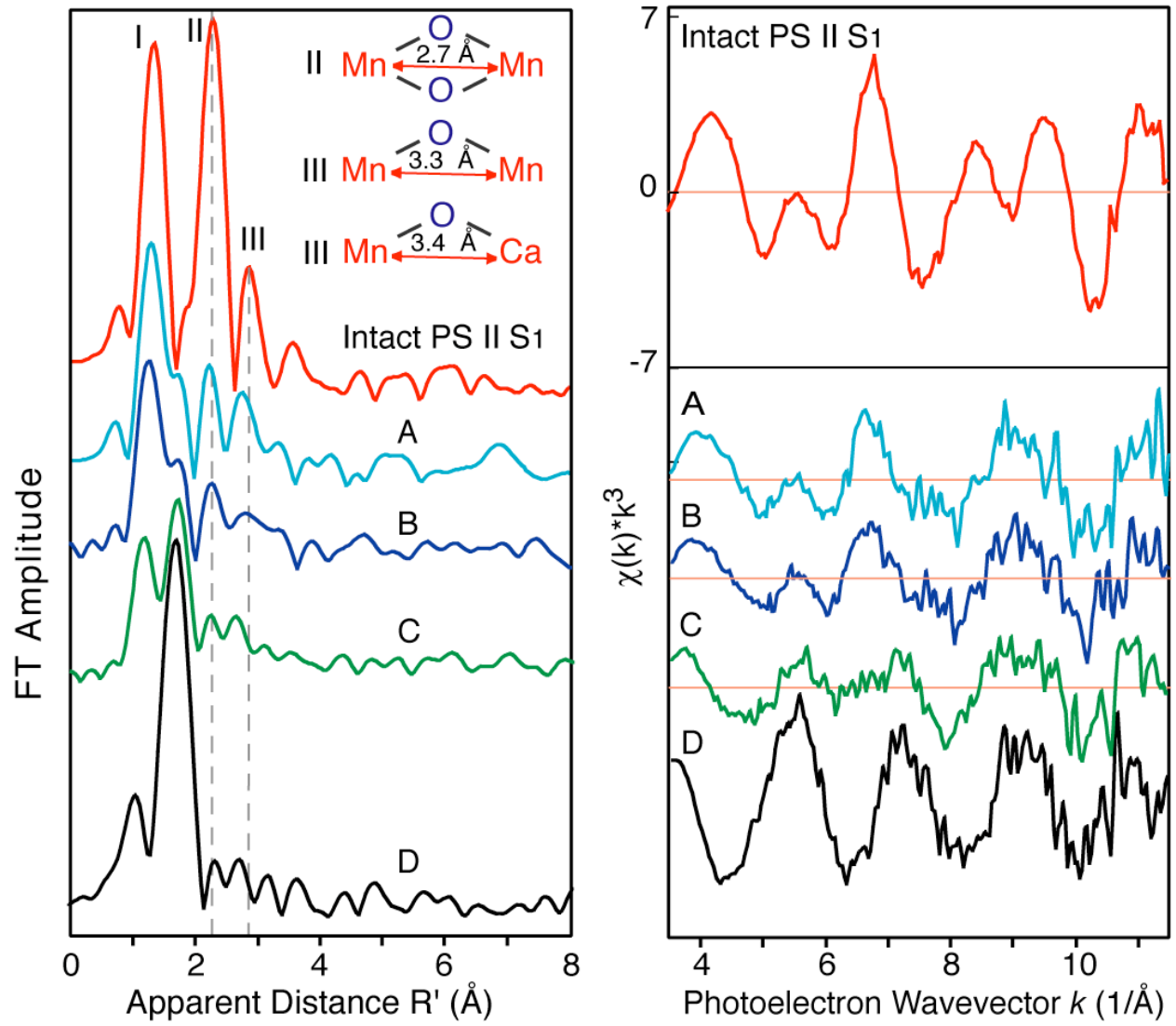
Figure 4

Figure 5

Figure 6

Figure 7

A

Model II

Model IIa

Model III

B

Figure 8

3.5 Å Structure
Ferreira et al (2004)

3.0 Å Structure
Loll et al (2005)

XAS Experimental Data

$\vec{e}$ // a
// b
// c
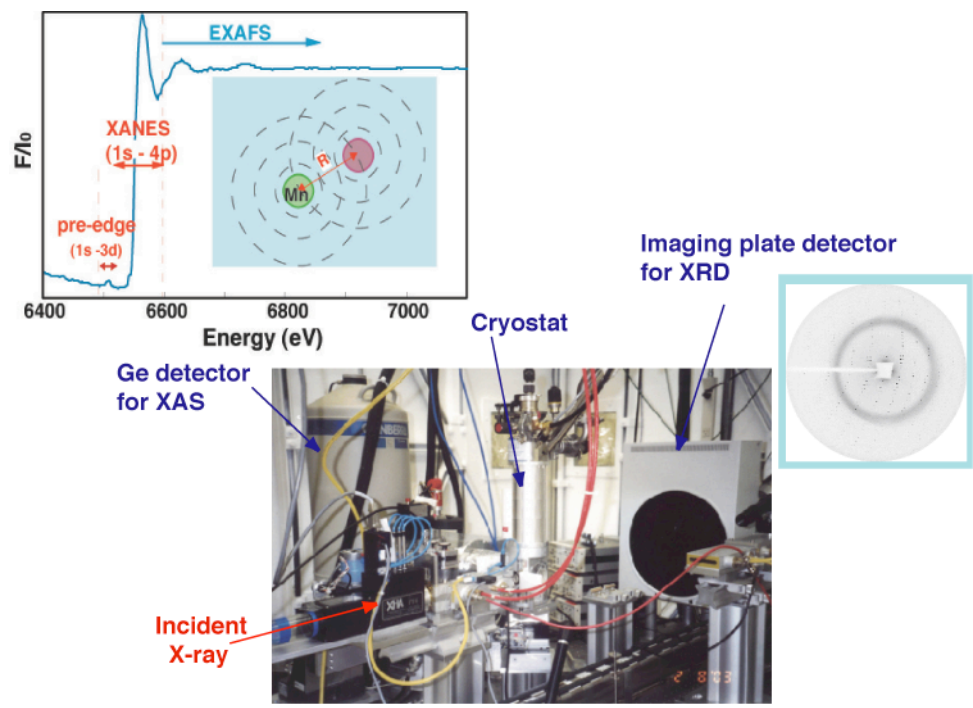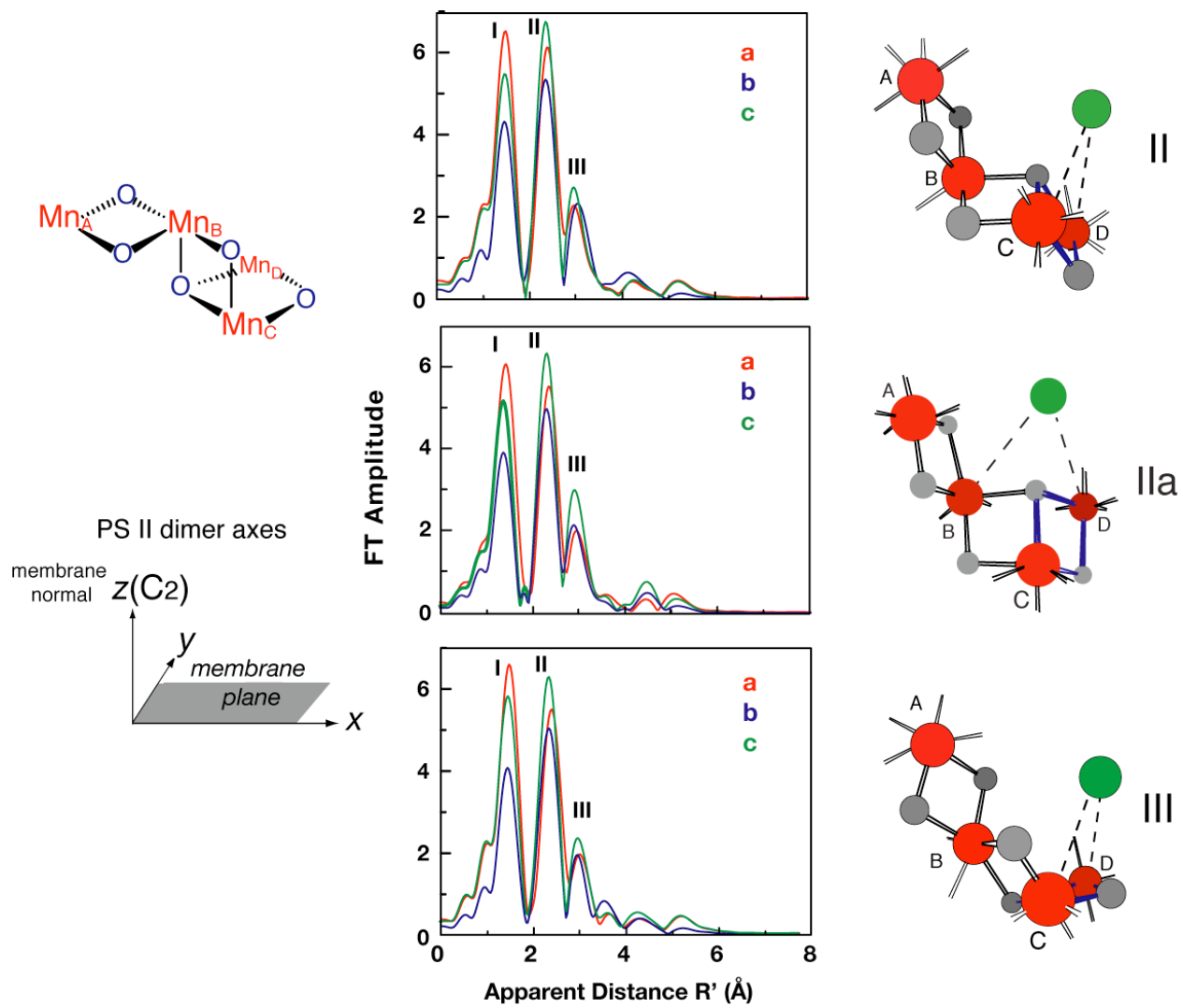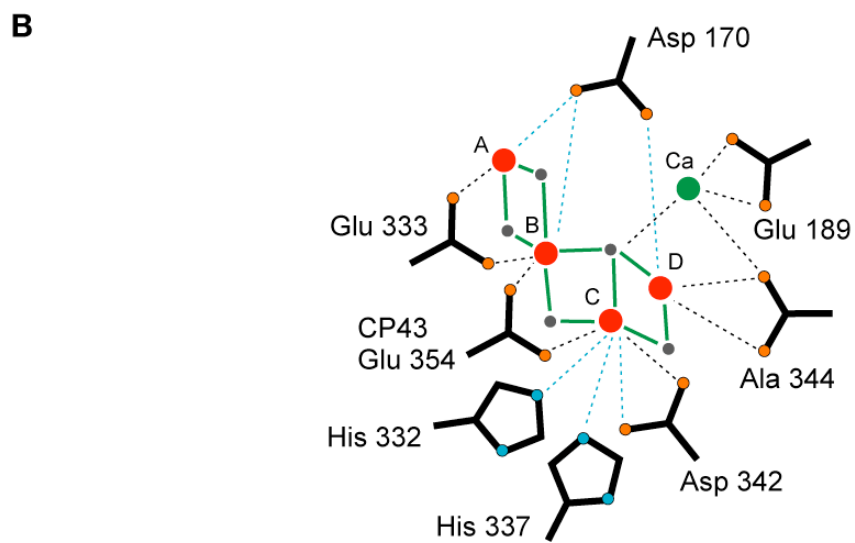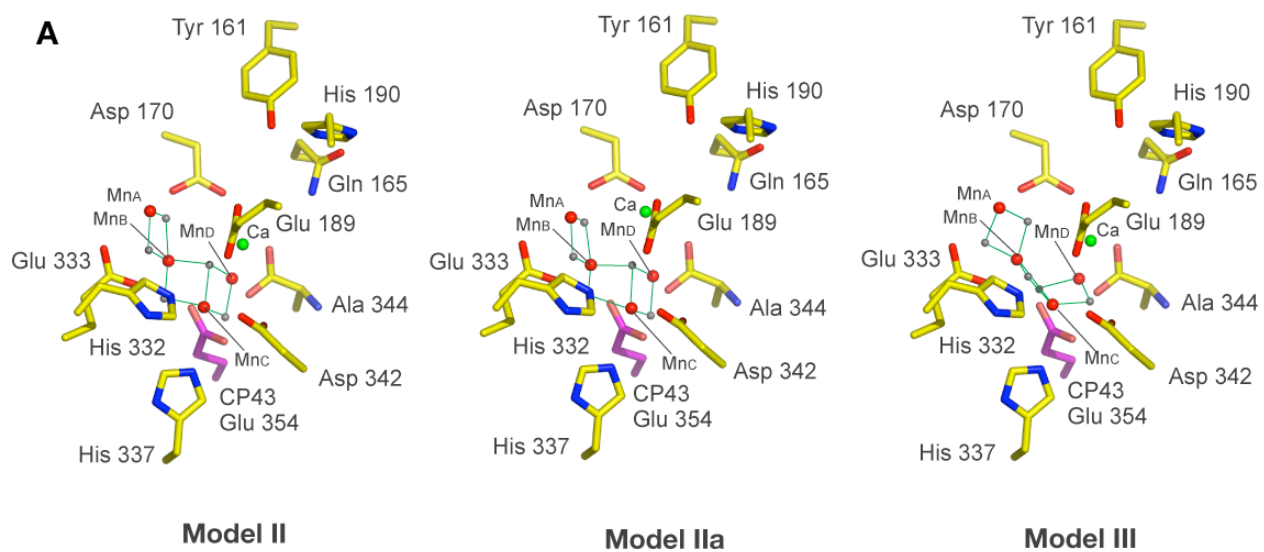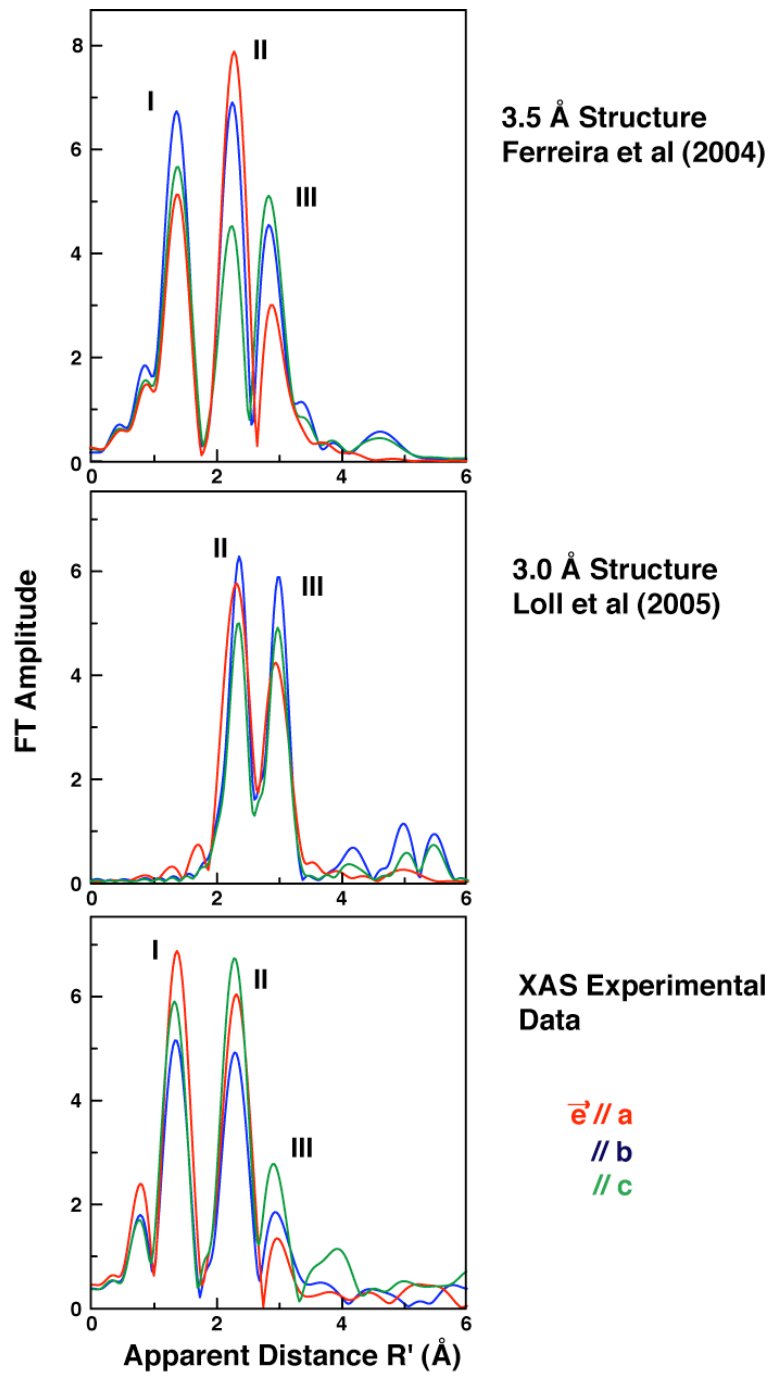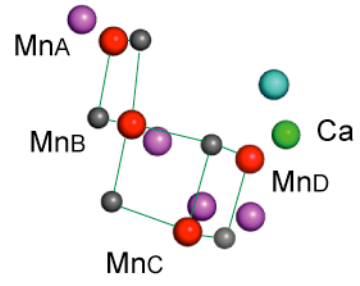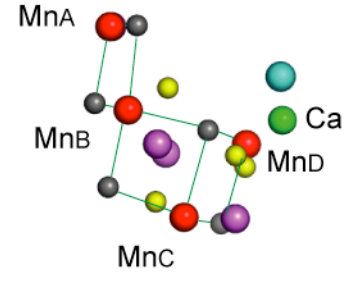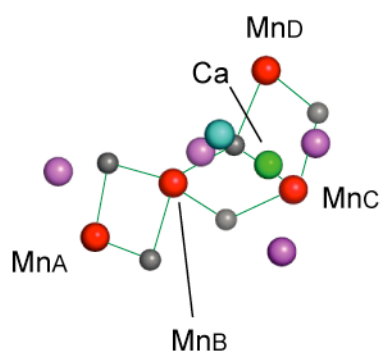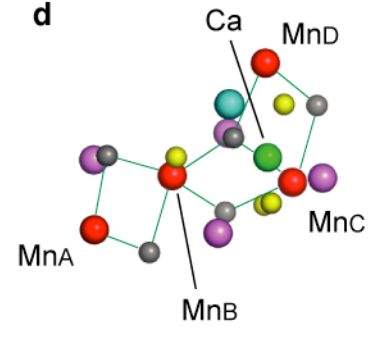
Figure 9A

Figure 9B

A
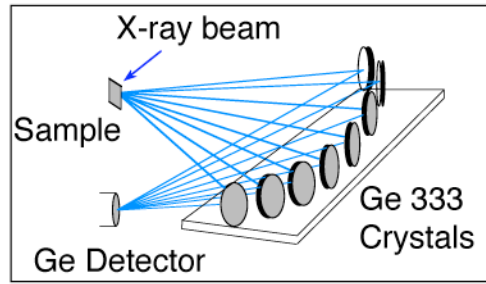
B
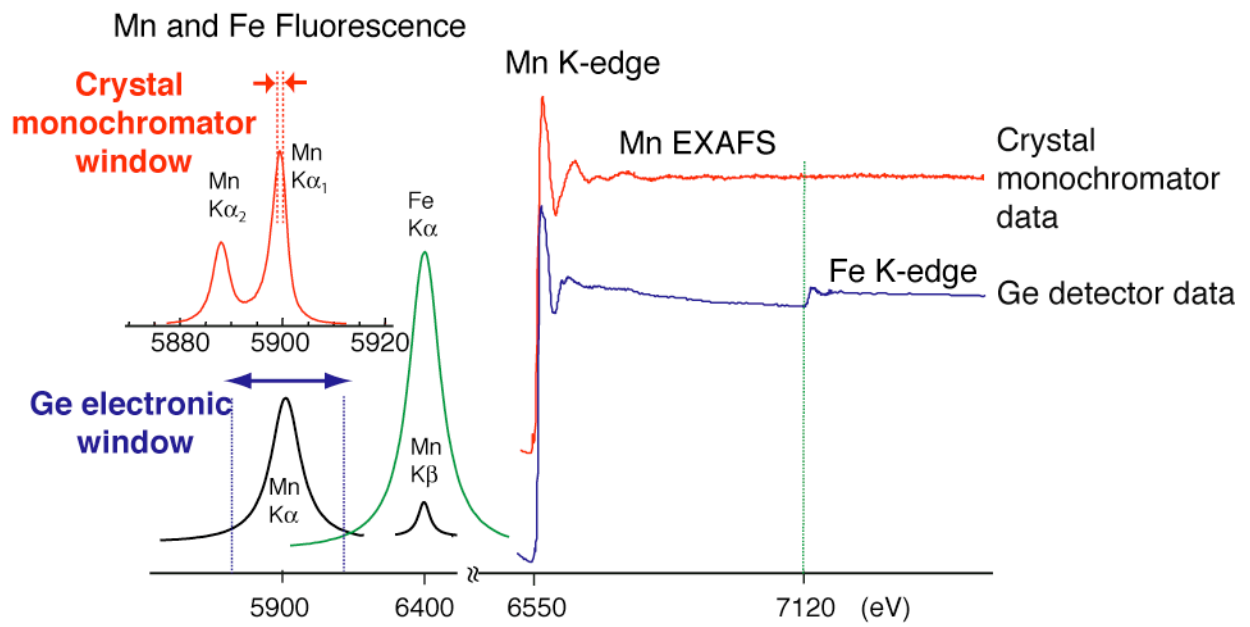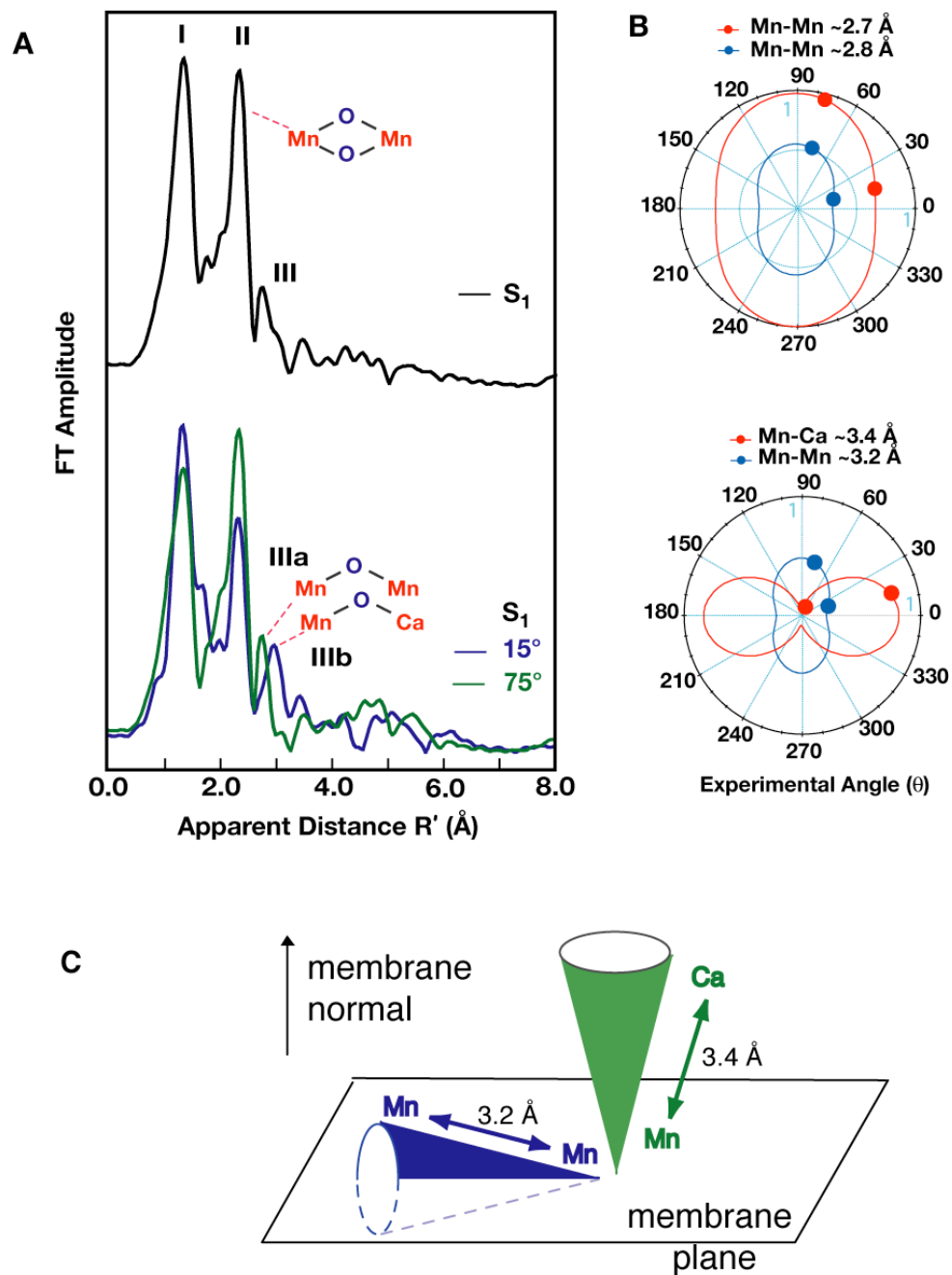
Figure 10

Figure 11

Figure 12

Figure 13

A Mn oxides
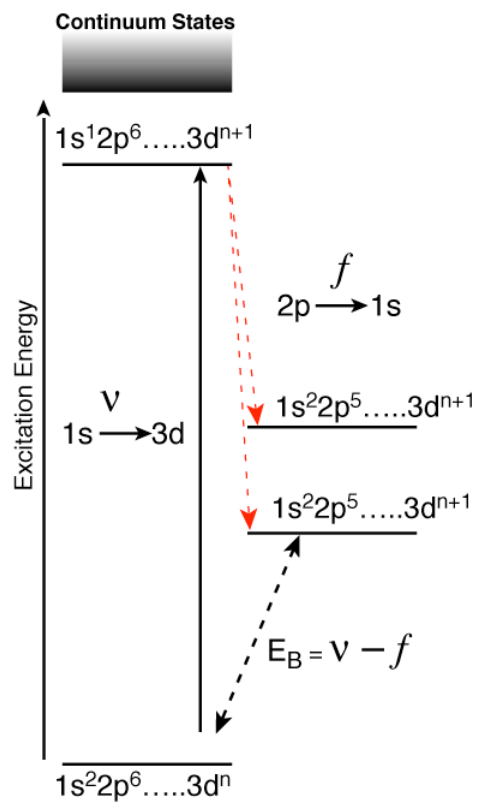

B Mn coordination complexes

C PS II
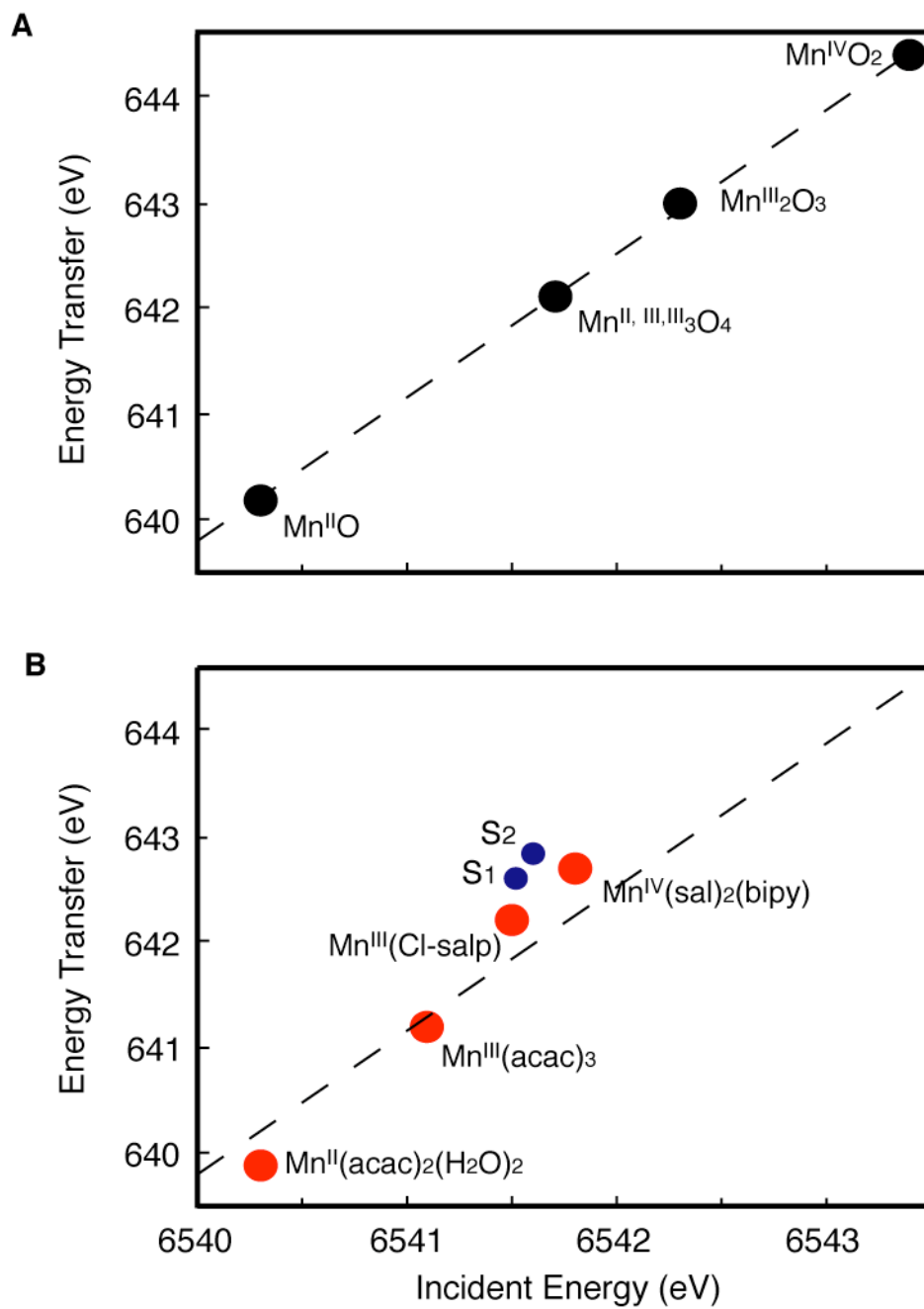

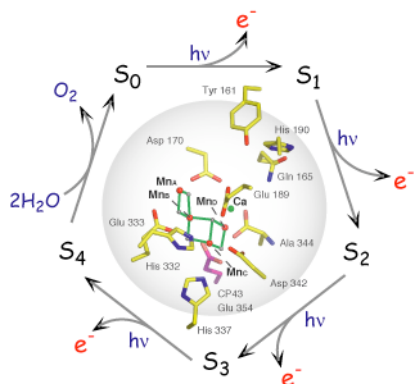**D** Cross Sections
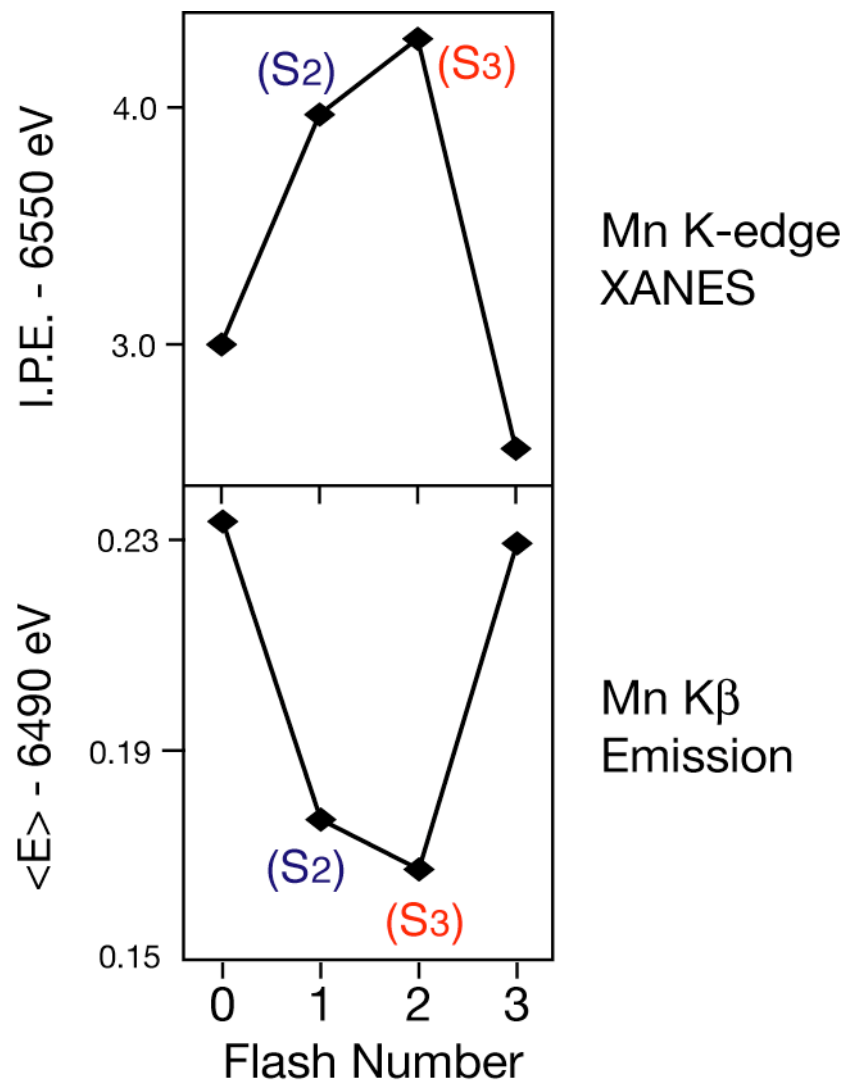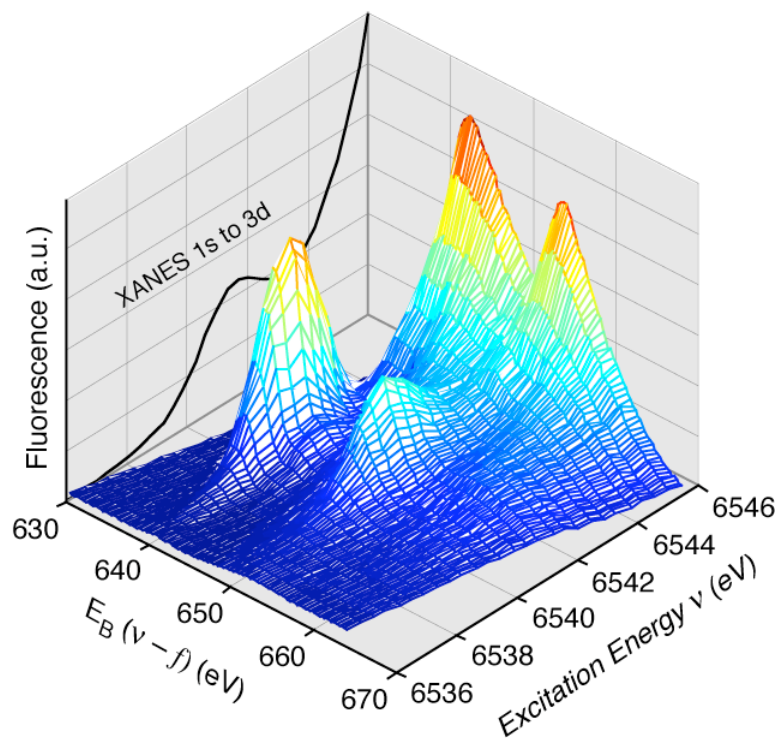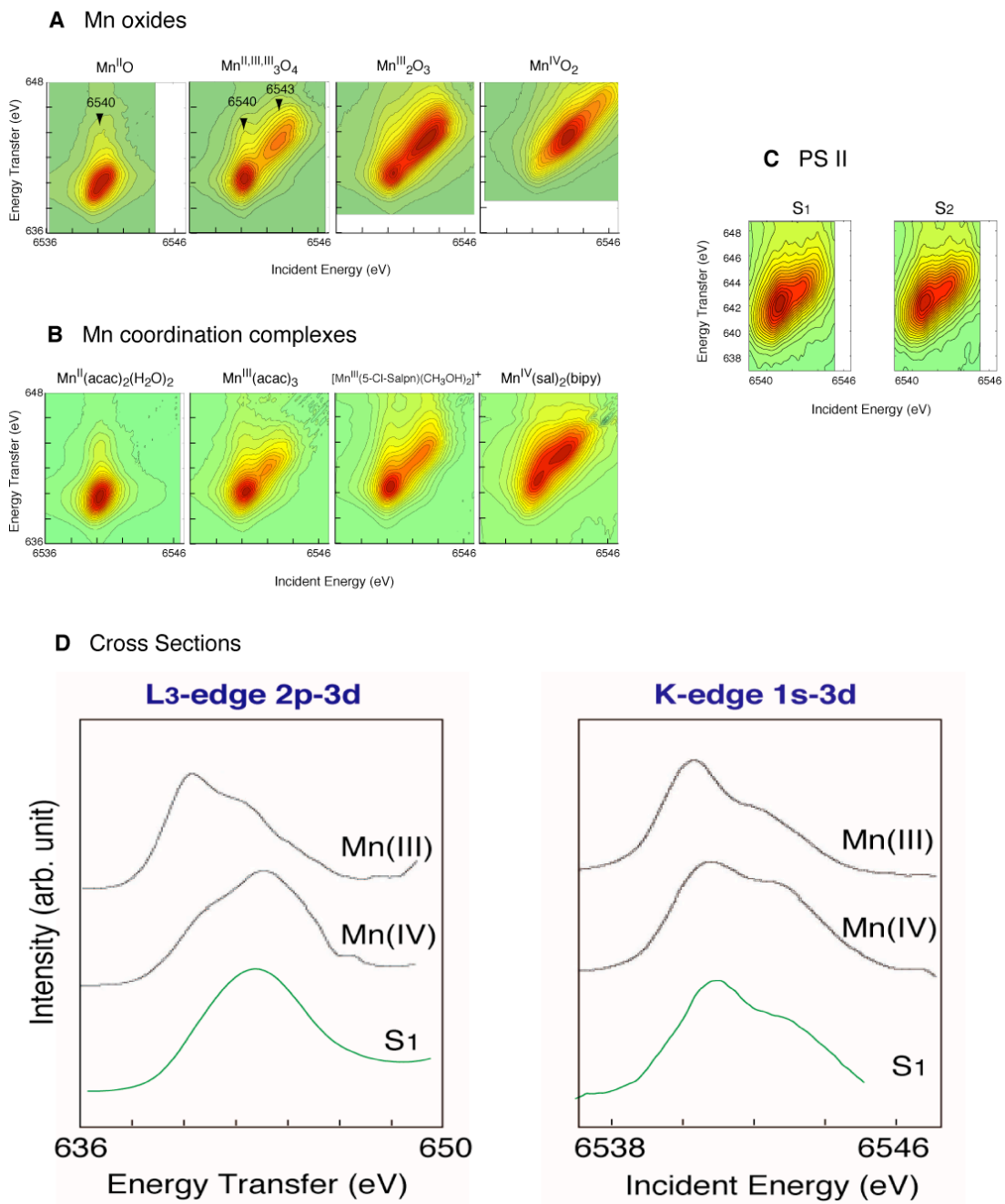
Figure 14

Figure 15

Table of Content Figure

Synopsis

Photosynthetic water oxidation is a fundamental chemical reaction that sustains the biosphere. This reaction is catalyzed by a Mn_4Ca cluster in photosystem II present in plants, algae and cyanobacteria. X-ray spectroscopy studies have been important for identifying the electronic and geometric structure of this complex and in determining the changes that are involved in the catalytic cycle, thus for understanding the basic principles that nature uses to oxidize water to dioxygen using light.